Low-speed Dynamic Wind Tunnel Test Analysis of a Generic 53° Swept UCAV Configuration with Controls

Dan D. Vicroy[1]
NASA Langley Research Center, Hampton, Virginia 23681, USA

Kerstin C. Huber[2] and Detlef Rohlf[3]
DLR, German Aerospace Center, D-38108 Braunschweig, Germany

and

Thomas Löser [4]
DNW, German-Dutch Wind Tunnels, D 38108 Braunschweig, Germany

Several static and dynamic forced-motion wind tunnel tests have been conducted on a generic unmanned combat air vehicle (UCAV) configuration with a 53° swept leading edge. These tests are part of an international research effort to assess and advance the state-of-art of computational fluid dynamics (CFD) methods to predict the static and dynamic stability and control characteristics for this type of configuration. This paper describes the dynamic forced motion data collected from two different models of this UCAV configuration as well as analysis of the control surface deflections on the dynamic forces and moments.

Nomenclature

|		
A	=	amplitude of oscillation
b	=	span
C_A	=	axial force coefficient
C_N	=	normal force coefficient
C_Y	=	side-force coefficient
C_l	=	rolling moment coefficient
C_{l_w}	=	wind axis rolling moment coefficient
C_m	=	pitching moment coefficient
C_{m_w}	=	wind axis pitching moment coefficient
C_n	=	yawing moment coefficient
C_{n_w}	=	wind axis yawing moment coefficient
c_r	=	root chord
$\bar{c}, c_{ref}$	=	reference chord
f	=	oscillation frequency
k	=	reduced frequency
p	=	roll rate
q	=	pitch rate
r	=	yaw rate
S_{ref}	=	reference area
t	=	time
V	=	velocity
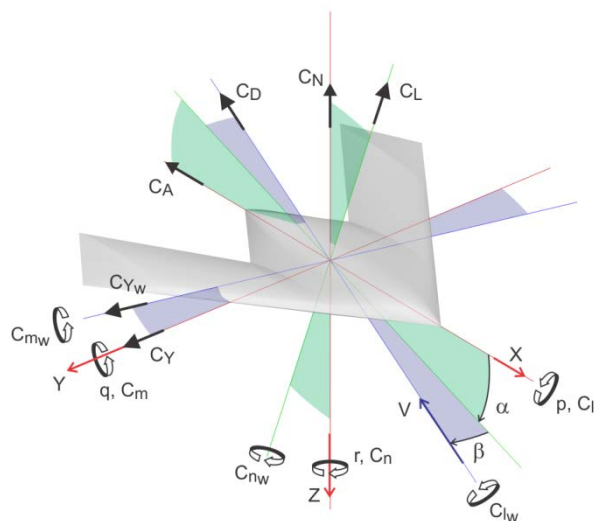
**Figure 1. Axes with force and moment orientation.**

---

[1] Senior Researcher, Flight Dynamics Branch, Research Directorate, MS 308, Associate Fellow, AIAA
[2] M.Sc., Research Scientist, DLR Institute of Aerodynamics and Flow Technology, Lilienthalplatz 7
[3] Research Scientist, Aircraft Division, Institute of Flight Systems, Lilienthalplatz 7
[4] Research Scientist, Low-Speed Wind Tunnel, Lilienthalplatz 7

α = AoA, angle of attack
$\dot{\alpha}$ = angle of attack rate
β = sideslip angle
$\dot{\beta}$ = sideslip angle rate
σ = standard deviation
ψ = yaw angle
θ = pitch angle
φ = roll angle
ω = angular velocity
DLR = German Aerospace Center (Deutsches Zentrum
           für Luft- und Raumfahrt)
DNW = German-Dutch Wind Tunnels (Deutsch-
           Niederländische Windkanäle)
LIB = left inboard
LOB = left outboard
LTIP = left tip
MRP = moment reference point
PIV = Particle Image Velocimetry
RIB = right inboard
ROB = right outboard
RTIP = right tip
SACCON = Stability and Control Configuration
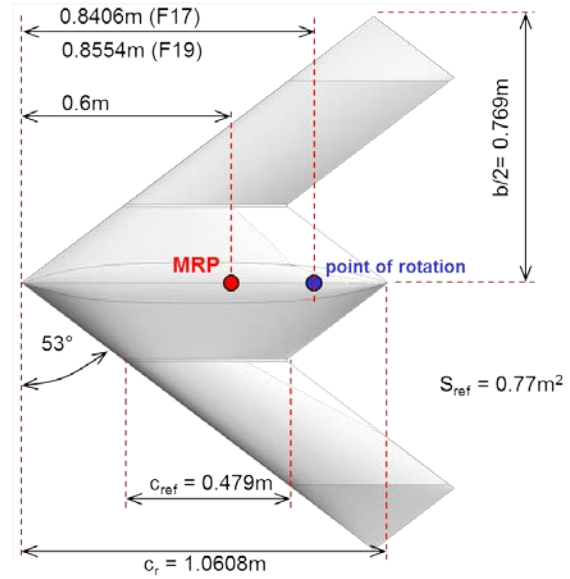
**Figure 2. Planform and geometric parameters of the generic UCAV configuration.**

I. Introduction

THIS paper is one of a series covering a North Atlantic Treaty Organization (NATO) led research effort exploring the capability of computational fluid dynamics (CFD) methods for stability and control analysis. This paper covers the dynamic wind tunnel tests of a generic unmanned combat air vehicle (UCAV) configuration. The CFD predictions will be compared with these experimental measurements in subsequent publications. This NATO Science and Technology Organization (STO) Applied Vehicle Technology (AVT) Task Group 201 builds on the research efforts of the predecessor task group AVT-161[1-9]. One of the additional emphasis of the AVT-201 is the prediction of deflected control surface effects. This paper describes the forced-oscillation experimental data from a series of wind tunnel tests of the generic UCAV configuration with multiple trailing edge control surfaces. A complementary set of static data has also been collected and is reported in reference 10.

II. Experimental Setup

A. UCAV Models

A generic UCAV configuration with a 53° leading edge sweep and a lambda wing planform, as shown in figure 2, was established as a focus configuration for the AVT-161 research. Two identically sized models of this configuration were built. The first was built by NASA and designated as the F17 **St**ability **a**nd **C**ontrol **Con**figuration (SACCON) while the second was built by DLR and designated the F19. The differences between the two models were primarily in the trailing edge control surfaces shown in figure 3. The F17/SACCON model was originally built without control surfaces but was later modified to include two 20% of reference chord trailing edge surfaces on the left or port wing. The SACCON model also had two different leading edge configurations, a sharp leading edge (SLE) and a round leading edge (RLE). The F19 model was built with the round leading edge geometry and trailing edge surfaces on both the right and left
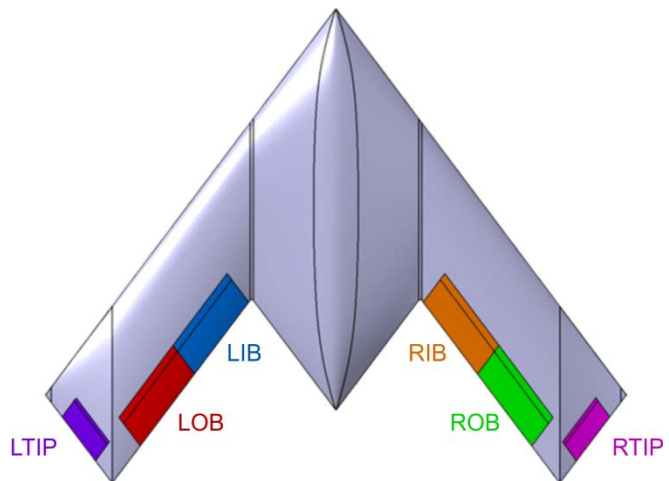
Figure 3. F19 control surface layout and designation.

2

wings that could be 20% or 25% chord. The F19 model was also included wing tip control surfaces. Control surface deflections were modeled with interchangeable fixed deflection parts.

Carborundum grit of size 60 was applied to approximately the first 25 mm at the nose to 10mm at the wing tip along both the upper and lower surface to provide fully turbulent flow across the models during both static and dynamic testing.

B. Wind Tunnels

All but one of the tests of the SACCON/F17 and F19 models were conducted in the DNW-NWB Low-Speed Tunnel located on the DLR site in Braunschweig, Germany. It is an atmospheric, closed circuit facility with a test section size of 3.25m by 2.80m, and can be operated with an open, closed or slotted test section[11]. The maximum free stream velocity in 2009 was V=80 m/s with the closed test section and V=70 m/s in the open test section. For the tests described in this paper, the closed test section was used.
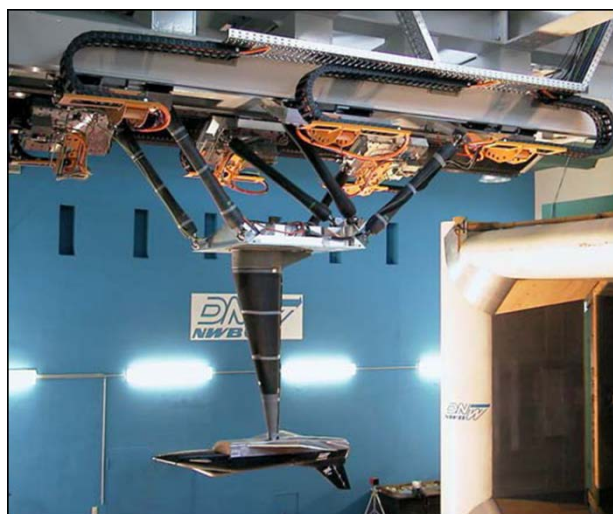
One of the tests of the SACCON/F17 model was conducted in the NASA Langley 14-by-22-Foot Subsonic Tunnel in Hampton, Virginia, USA. This is also an atmospheric, closed circuit facility. The test section is 4.42 m by 6.63 m with a maximum free stream velocity of V=106 m/s.

C. Forced Motion Systems

1. MPM System (DNW-NWB)

DNW-NWB's Model Positioning Mechanism (MPM) is a six degree-of-freedom (DOF) parallel kinematics system designed for static as well as for dynamic model support[12,13]. Characteristic features of this unique test rig are the six constant length struts of ultra-high modulus carbon fiber and the six electric linear motors, which traverse along two parallel rails above the test section. The MPM can be operated in the open or closed test section configuration. The MPM can be used for high precision static model positioning as well as for sinusoidal oscillations and arbitrary multi-axes maneuvers. The model location and orientation in the tunnel are determined in real time through an optical photogrammetric system featuring two high speed video cameras mounted below the test section. Increased pitch or bank angle range can be obtained with an additional electric actuator and pushrod mounted on the moveable (Stewart) platform to actuate the additional motion. The MPM oscillation frequency can be set continuously from 0.0 to 3.0 Hz. The amplitude range depends, among other parameters, on the frequency, the oscillation type and the balance mount geometry.

Figure 4. X-31 model on the MPM in the open test-section of DNW-NWB.

The MPM with the X-31 model installed is shown in figure 4. Although the figure shows an open test section, the SACCON/F17 and F19 tests were conducted in the closed configuration. With the closed test section the Stewart platform remains outside the test cell and only the sting protrudes through a movable hatch into the test section wall.

D. Dynamic Wind Tunnel Tests

A summary of all the dynamic wind tunnel tests conducted is provided in table 1. The three tests conducted in 2009 in both the DNW-NWB and NASA tunnel were focused on amplitude and frequency effects on the dynamic derivatives of the F17/SACCON model without control defelctions.[3,4] The DNW-NWB test T2426 focused on conducting particle image velocimetry (PIV) measurements of the off-body flow characteristics at various attitudes and for a very limited set of pitch oscillations. These PIV are presented in references 5 and 6, and are not included in the analysis of this paper. This paper focuses on the effect of control deflections on the dynamic derivatives on the F17/SACCON and F19 models. No roll axis forced motion was conducted for the F19 model.

Table 1. Summary of generic UCAV dynamic wind tunnel tests.

Date	Tunnel	Test #	Model	Controls	Motion				
					Roll	Pitch	Yaw	Plunge	Maneuver
1/2009	DNW-NWB	2373	F17/SACCON	No		●	●	●	
3/2009	DNW-NWB	2426	F17/SACCON	No		●			
11/2009	NASA 14x22	134	F17/SACCON	No	●		●		
12/2011	DNW-NWB	2514	F17/SACCON	Yes	●	●	●		
5/2012	DNW-NWB	2540	F17/SACCON	Yes	●	●	●		
5/2013	DNW-NWB	2545	F19	Yes		●	●		●

E. Data Processing

The force and moment balance signals were sampled at 600 Hz in the DNW-NWB tests and 300 Hz in NASA 14x22-foot test. All balance signals were passed through a low-pass filter with a cut-off frequency of 5 Hz.

There were no corrections for wall or blockage effects applied to the forced motion time history data. The DNW-NWB static data is available both with and without wall and blockage corrections. For comparison purposes, all of the data presented in this paper (both static and dynamic) are without wall or blockage corrections. The model blockage at 30° AoA is 4.0% in the DNW-NWB tunnel and 1.3% in the NASA 14x22-foot tunnel.

The NASA static and forced oscillation data were corrected for sting bending. The model attitude in the DNW-NWB tests was measured optically so no sting bending correction was required.

2. One Cycle Averaging

The sinusoidal dynamic data runs consisted of at least 30 seconds of multi-cycle measured forces, moments, model position and pressures. Each multi-cycle sinusoidal data run was later condensed to a one cycle average loop with standard deviation about fixed oscillation phase angle values. Figure 5 shows an example of a 1Hz pitch oscillation pitching moment data set for the SACCON/F17 model. The nominal AoA is 20° with a pitch amplitude of 5°. Also shown in the figure are the static data and the 1-cycle average with standard deviation bars. The coefficient values at the nominal value crossing points are of particular interest. At these points in the oscillation cycle the rotational acceleration is zero and the rotation rate is the maximum and minimum. Of note is the growth in the standard deviation of the oscillation loop in the higher AoA region of unsteady aerodynamics. An objective of AVT-161 and follow-on AVT-201 task groups is to assess the ability of current CFD methods to model the physics required to replicate these 1-cycle averaged loops.
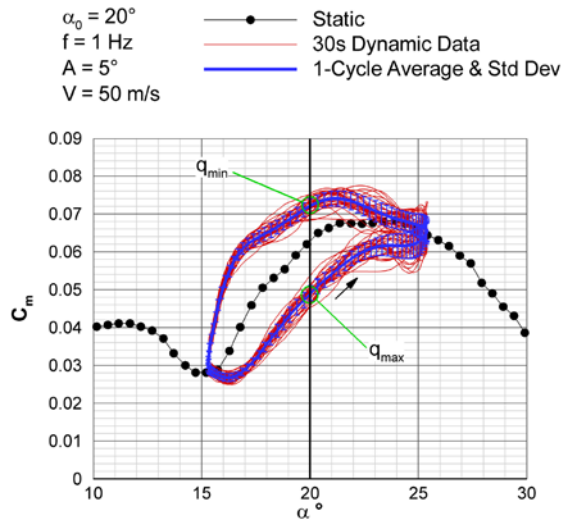

Figure 5. Example muti-cycle pitch oscillation time history of pitching moment coefficient vs. AoA.

3. Dynamic Derivative Analysis

Beyond the tunnel corrections and 1-cycle averaging some additional data processing was conducted to assess the classic dynamic derivatives from the forced oscillation data. The sinusoidal roll, pitch and yaw oscillations include both body and velocity vector rotation rates. For example, the pitch oscillation motion has both pitch rate (q) and AoA rate ($\dot{\alpha}$). From this type of motion, a combined derivative is generally derived, such as:

$$\overline{C_{m_q}} = C_{m_q} + C_{m_{\dot{\alpha}}} \tag{1}$$

The rolling and yawing oscillations produce combined derivatives which include sideslip rate terms.

$$\overline{C_{l_p}} = C_{l_p} + C_{l_{\dot{\beta}}} \sin \alpha \tag{2}$$

4
American Institute of Aeronautics and Astronautics

$$\overline{C_{n_r}} = C_{n_r} - C_{n_{\dot{\beta}}} \cos \alpha \tag{3}$$

To split the combined derivative into the individual terms requires motions with only one of the rotation rates such as plunging, which has no pitch rate.

One method of deriving the combined dynamic derivatives from the oscillation data, often referred to as the "single point" method, is to compute the difference of the maximum and minimum rate coefficient values divided by the difference in the maximum and minimum rates[14,15]. For example:

$$\overline{C_{m_q}} = \frac{C_{m_{(q_{max})}} - C_{m_{(q_{min})}}}{\frac{\bar{c}}{2V}(q_{max} - q_{min})} \tag{4}$$

Some examples of the combined dynamic derivatives computed in this manner are presented in the "Results and Discussion" section.

4. Analysis of Pitch Maneuver Data

A series of pitch maneuver runs were also conducted with the F19 model that took advantage of the dynamic motion capabilities of the MPM. These maneuvers consisted of either steady pitch sweeps of various rates, or pitch sweeps with an overlaid 5° pitch oscillation at varying frequencies. For example, the angle-of-attack and non-dimensional pitch-rate, and resultant pitching moment coefficient time-history of three of these maneuvers appended together is shown in figure 6. This data was collected for a DLR research project in advanced dynamic modeling and parameter identification and was not originally intended for inclusion in this paper. However, a simple linear dynamics model was fit to these maneuver datasets and yielded useful results for this AVT-201 research.

An aerodynamic coefficient model was assumed to be comprised of a static and a dynamic term that are functions of angle-of-attack. For example:

$$C_m = C_{m_{static}}(\alpha) + C_{m_{dyn}}(\alpha) = C_{m_{static}}(\alpha) + \left(\frac{q\bar{c}}{2V}\right)\overline{C_{m_q}}(\alpha) \tag{5}$$
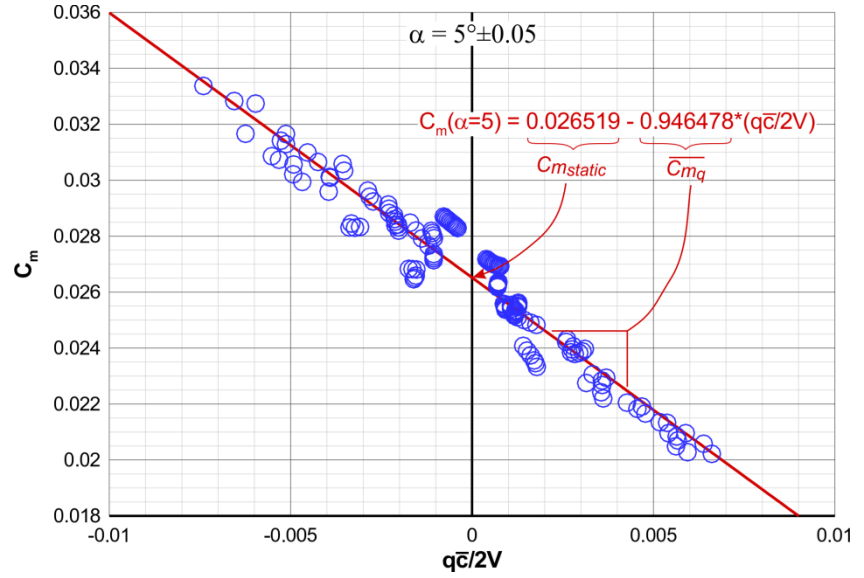
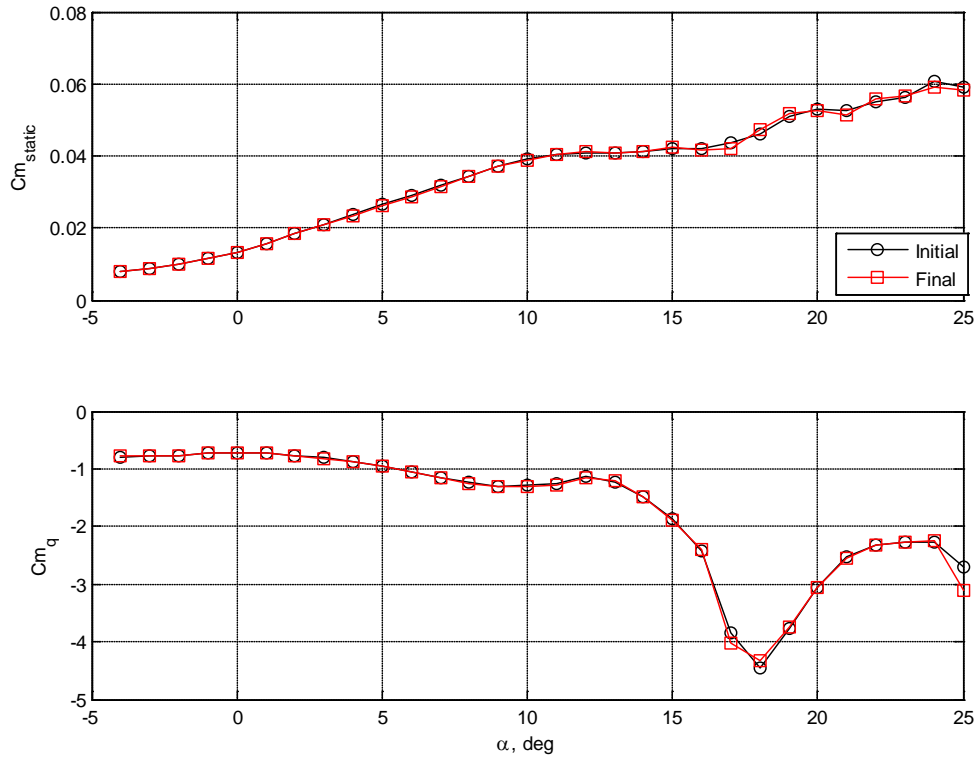This linear dynamic model was fit to the maneuver data as follows:
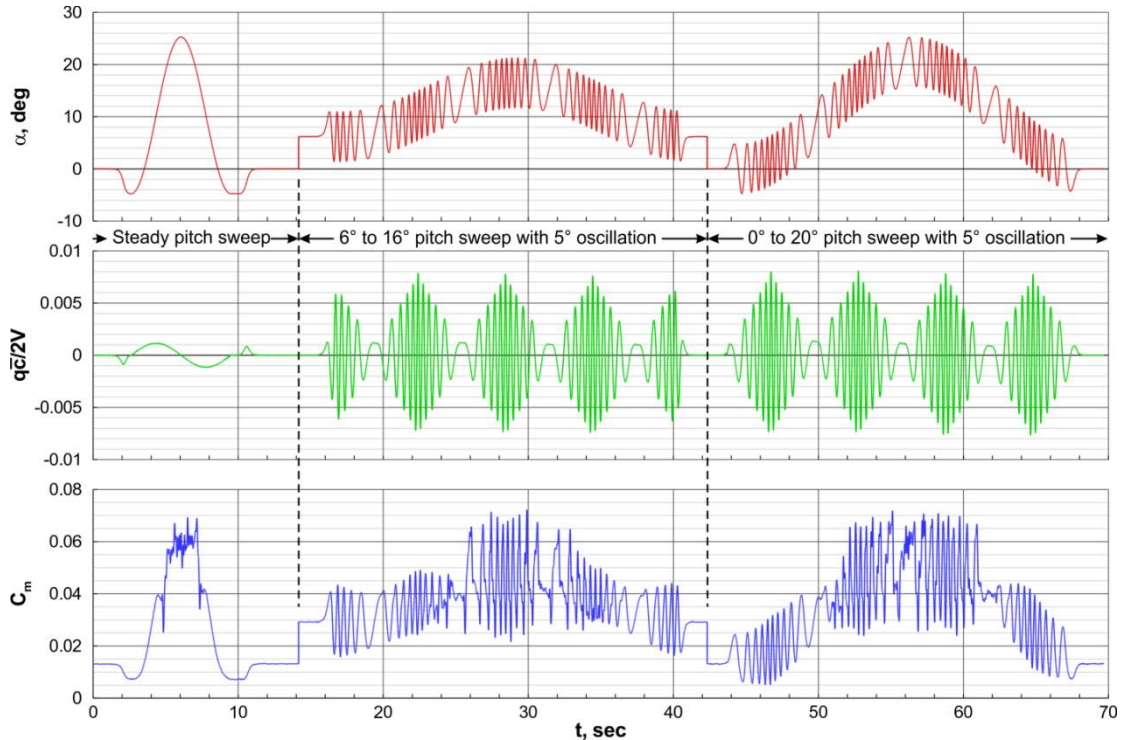
Figure 6. Example of three appended pitch maneuver time histories.

5

American Institute of Aeronautics and Astronautics

a) The maneuver data was binned by angle-of-attack in 1-degree intervals from -4 to 25 degrees with a tolerance of ±0.05 degrees.

b) For each binned angle of attack a least-squares linear fit of the force and moment coefficient data with non-dimensional pitch rate was generated. For example, figure 7 shows the pitching moment coefficient data from the figure 6 maneuver collected about an angle of attack of 5±0.05 degrees with the

Figure 7. Linear fit of pitching moment coefficient with non-dimensional pitch rate from maneuver data at $\alpha = 5° \pm 0.05$.

corresponding non-dimensional pitch rate. The slope of the liner fit provides the dynamic term $\overline{C_{m_q}}(\alpha = 5)$ and the intercept is the static term $C_{m_{static}}(\alpha = 5)$. The result is 30 static and dynamic terms for each force and moment coefficient model corresponding to the integer angle of attack values from -4 to 25 degrees.

c) These 30 static and dynamic values were then used as the starting values for a least-squared fit optimization of the coefficient model to the entire maneuver time history to see if further refinement could be achieved. The model used linear interpolation between angle of attack node points. An


Figure 8. Initial and final pitching moment model fit values with angle of attack.

6

example of the initial model coefficient values and the final optimized values along with the maneuver time history fit comparisons are shown in figures 8 - 10. In general, the optimization yielded very little difference in the model coefficient values. The largest model fit differences were at the higher angles of attack where the aerodynamics are more nonlinear and unsteady, and the model structure may be insufficient. This is illustrated in figure 10, which shows the pitching moment coefficient model fit error with angle of attack and non-dimensional pitch rate.
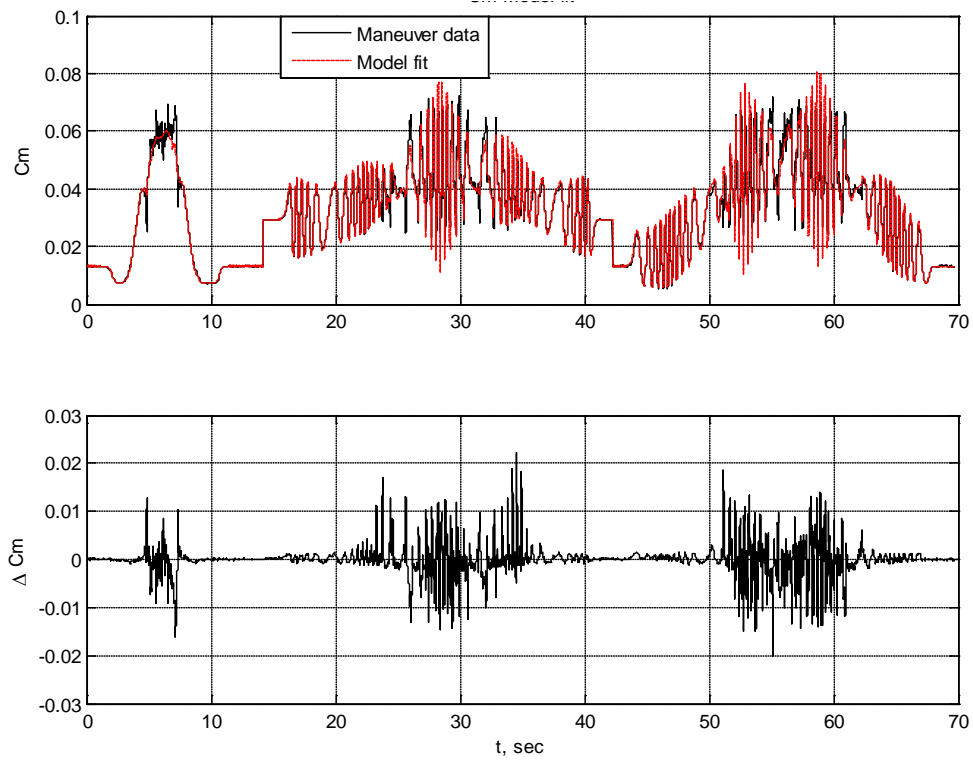
Figure 9. Pitching moment coefficient model comparison with maneuver time history data.
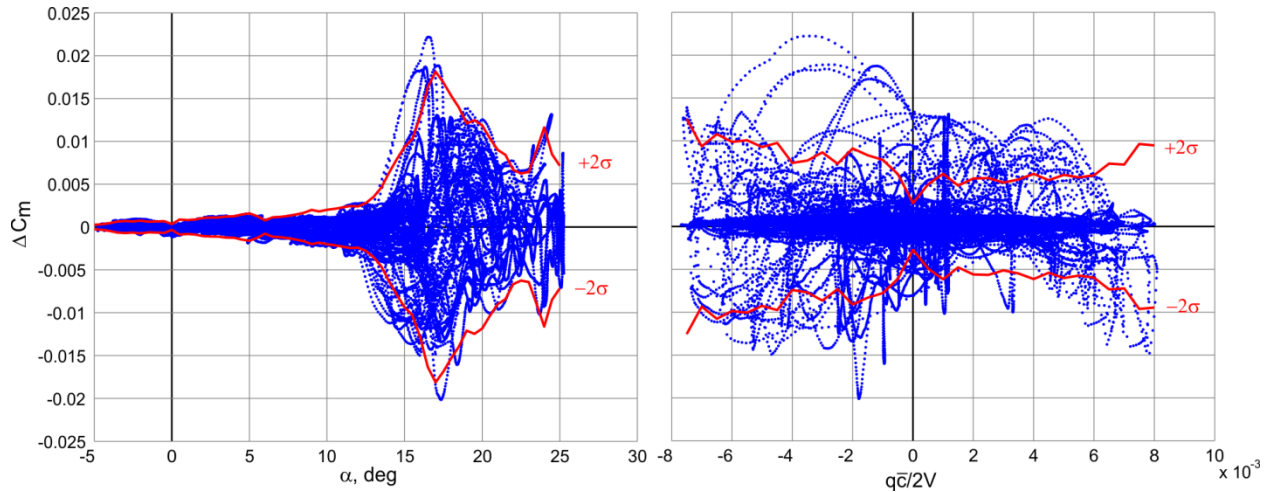
Figure 10. Pitching moment fit residuals with angle of attack and non-dimensional pitch rate.

American Institute of Aeronautics and Astronautics

III. Results and Discussion

The breadth of dynamic data collected during the six wind tunnel tests of the SACCON/F17 and F19 models exceeds what can be fully examined within the scope of this paper. The effects of velocity, oscillation frequency and amplitude were previously examined in references 4 and 8. This paper will focus on the effects of the UCAV control deflections on the dynamic derivatives.

F. Test to Test, Tunnel to Tunnel and Model to Model Comparisons

Comparisons of the dynamic data from test to test as well as between the two geometrically similar models were conducted. These comparisons were without control deflections and with the gaps between control surfaces sealed with tape. Comparisons of the SACCON/F17 and F19 dynamic data were only available for the pitch and yaw axis.

5. Pitch axis comparisons

Figures 11 and 12 show comparisons of the pitch axis dynamic derivatives for both the SACCON/F17 and F19 models plotted over several tests conducted in the DNW-NWB tunnel for oscillation frequencies of 1 and 2 Hz, respectively. Both models provided similar results with the largest variations occurring in the pitch damping derivative ($\overline{C_{m_q}}$) at angles of attack of 15° and above. The 15° angle of attack 1-cycle averaged hysteresis loops shown in figures 13 and 14 provide some insight into the source of the damping derivative variation. The damping derivative is proportional to the thickness of the hysteresis loop at the zero $\Delta\theta$ axis intersection. Although the shape of the pitching moment loops are similar their thickness changes rapidly near the zero axis resulting in large variations in the derivatives in this angle of attack region.

6. Yaw axis comparisons

Test to test comparisons of the yaw axis dynamic derivatives measured in the DNW-NWB tunnel are shown in figure 15. In general, the yaw axis derivatives are very small due to the lack of vertical surfaces on the all wing configuration. Similar to the pitch axis, the yaw axis derivatives show good agreement at the lower angles of attack with larger variations at 15° and above. There is also a notable difference between the F19 and SACCON/F17 $\overline{C_{Y_r}}$ and $\overline{C_{l_r}}$ values at 20° angle of attack. Figure 16 shows the 1-cycle average hysteresis loops for this angle of attack. Both the side force and rolling moment hysteresis loops for the F19 model are considerably thicker than the others resulting in the larger derivative magnitudes shown in figure 15. These variations could be due to small differences between the models that affect the separation characteristics at this higher angle of attack.

7. Roll axis tunnel to tunnel comparisons

Roll axis oscillations were conducted in both the DNW-NWB and NASA 14- by 22-Foot tunnels but, as previously noted, the these tests were only conducted with the SACCON/F17 model. The model mounting configurations for the roll axis oscillations in the two tunnels were considerably different as shown in figure 17. The DNW-NWB tests used a belly mount with a "seventh-axis" push rod to oscillate the model whereas the NASA test used and aft sting mount. This difference in the mounting arrangement however did not have a significant effect on the roll axis dynamic derivatives as shown in figure 18.
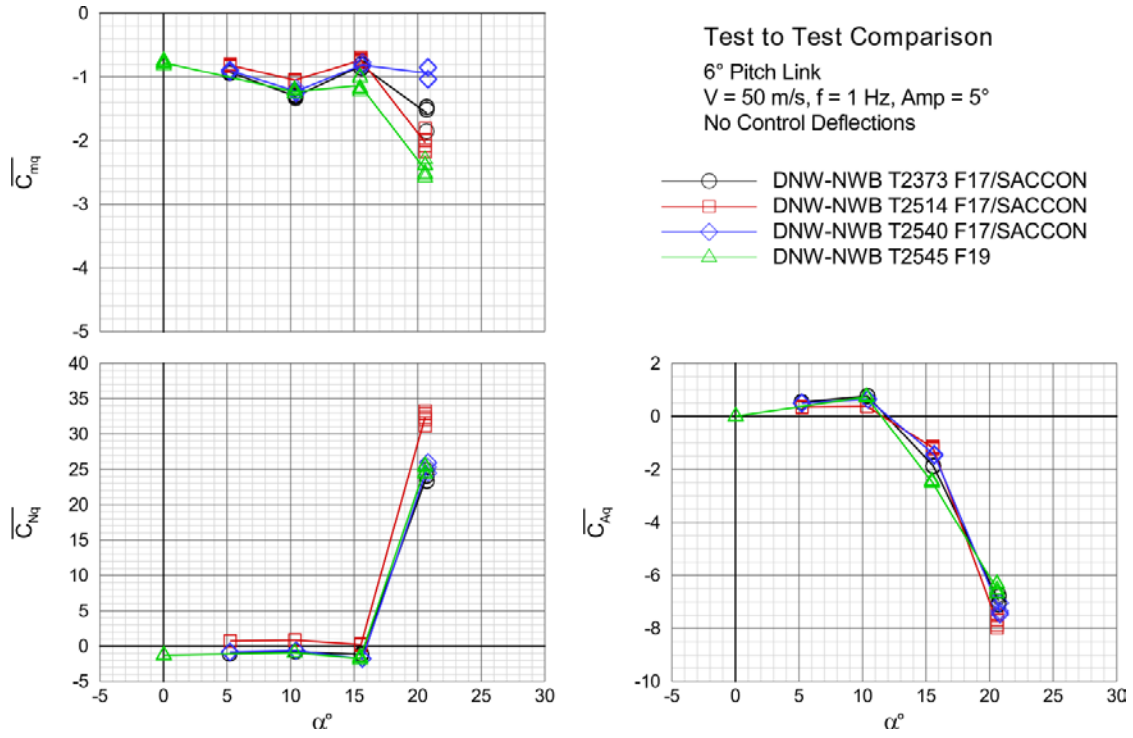
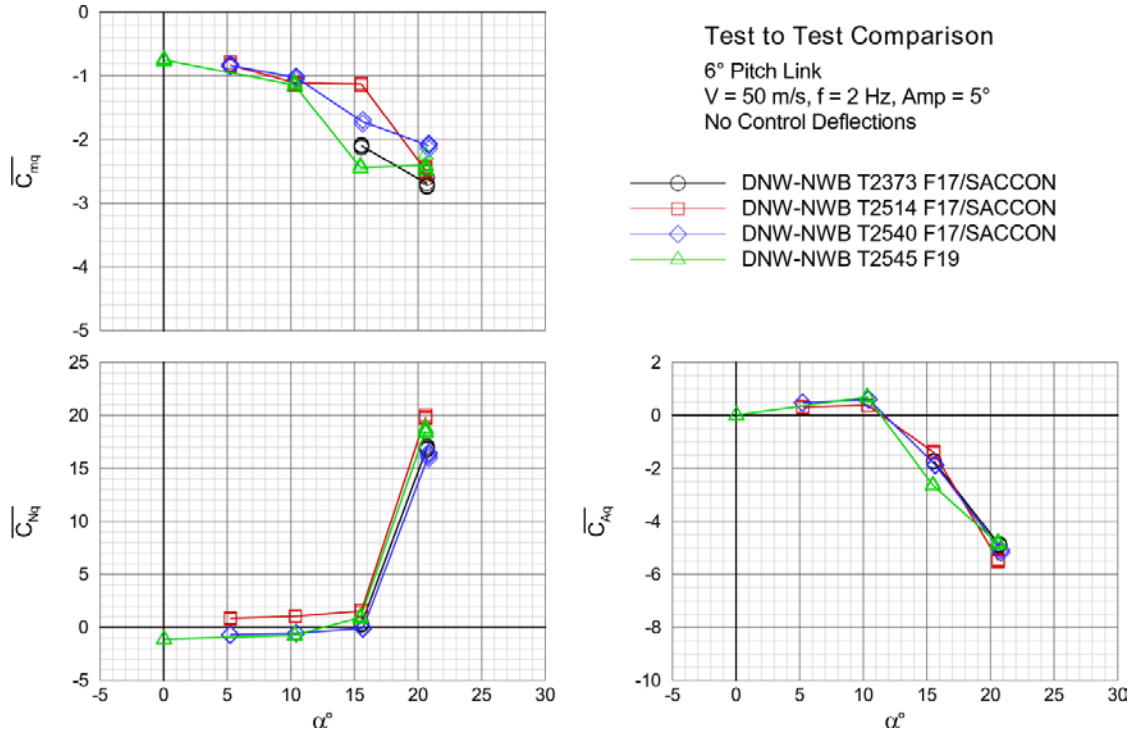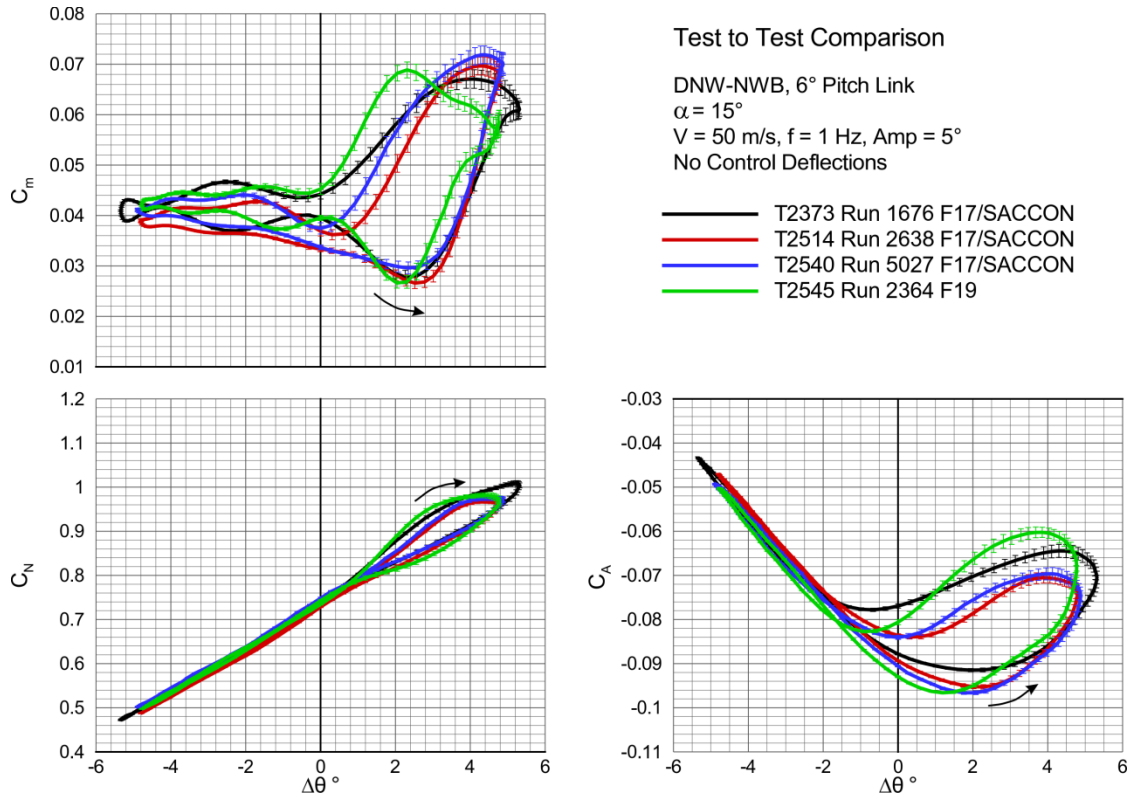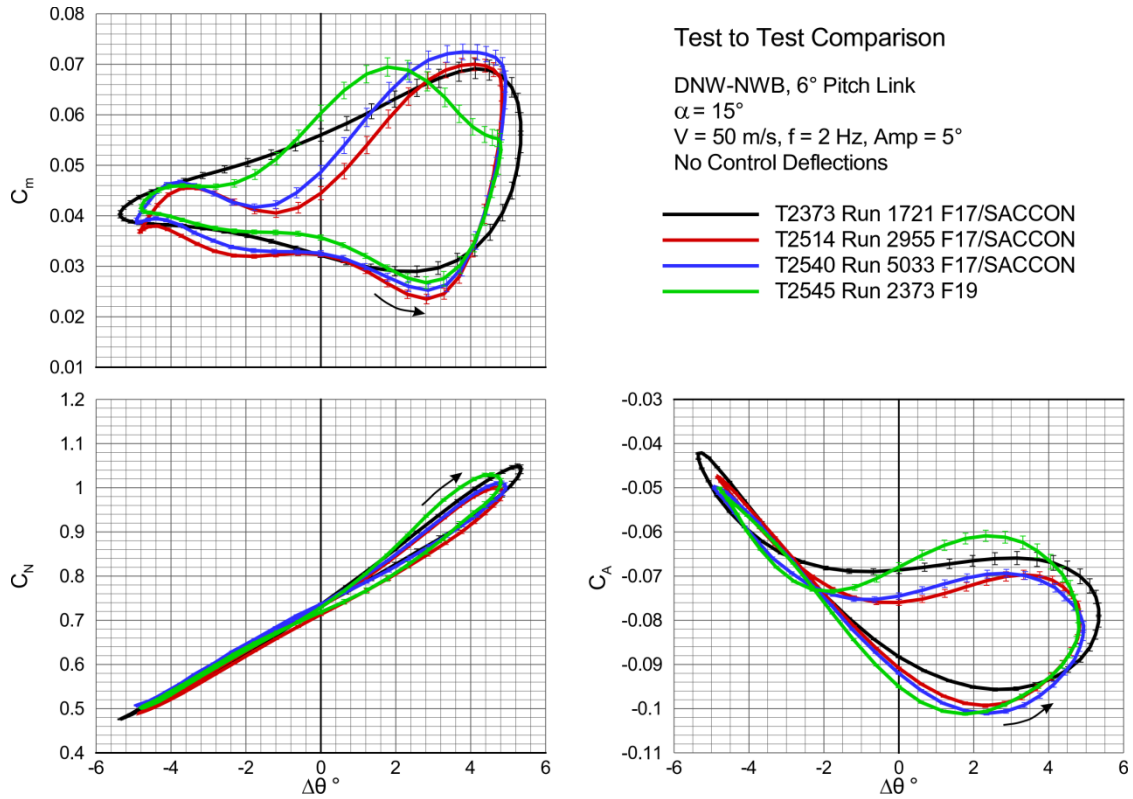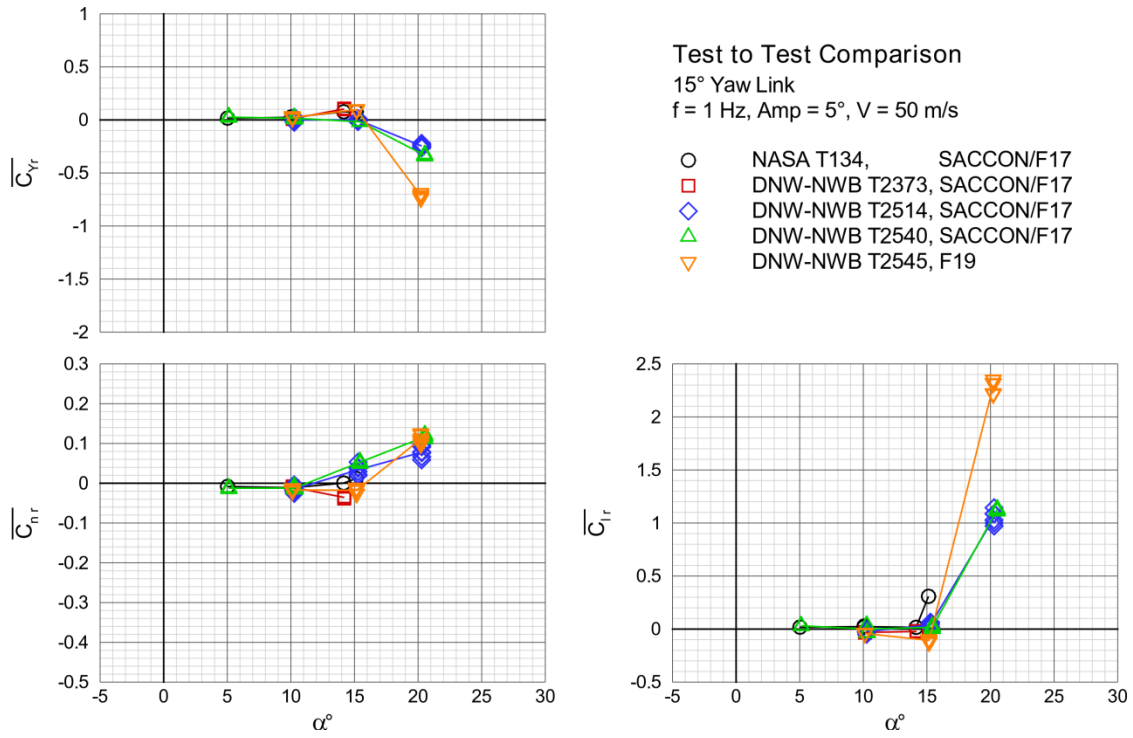**Figure 11.   Comparison of pitch axis dynamic derivatives for 1 Hz oscillation frequency.**

Figure 12.   Comparison of pitch axis dynamic derivatives for 2 Hz oscillation frequency.

American Institute of Aeronautics and Astronautics

Figure 13. **1-cycle average pitch hysteresis loop with standard deviation bars for 1 Hz oscillation.**

Figure 14. **1-cycle average pitch hysteresis loop with standard deviation bars for 2 Hz oscillation.**

American Institute of Aeronautics and Astronautics

Figure 15. Test to test comparison of yaw axis dynamic derivatives for 1 Hz oscillation frequency.
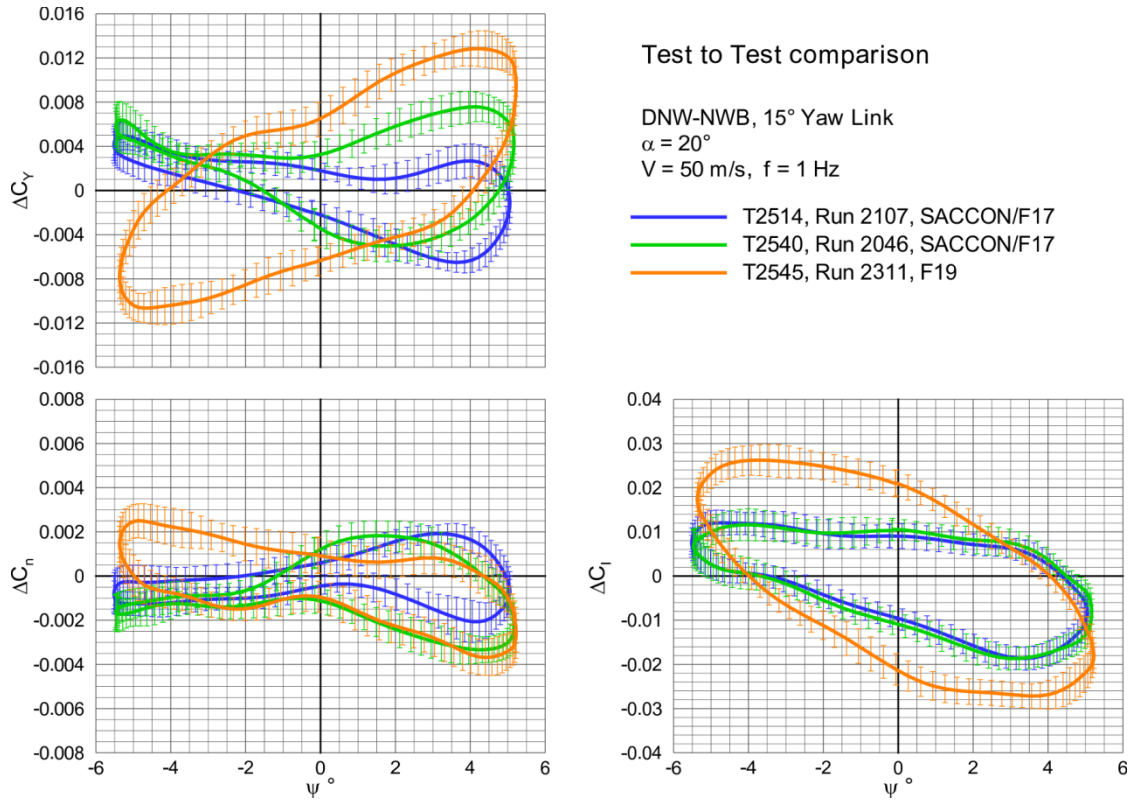
Figure 16. Test to test comparison of 1-cycle average yaw hysteresis loop with standard deviation bars for 1 Hz oscillation at 20° angle of attack.
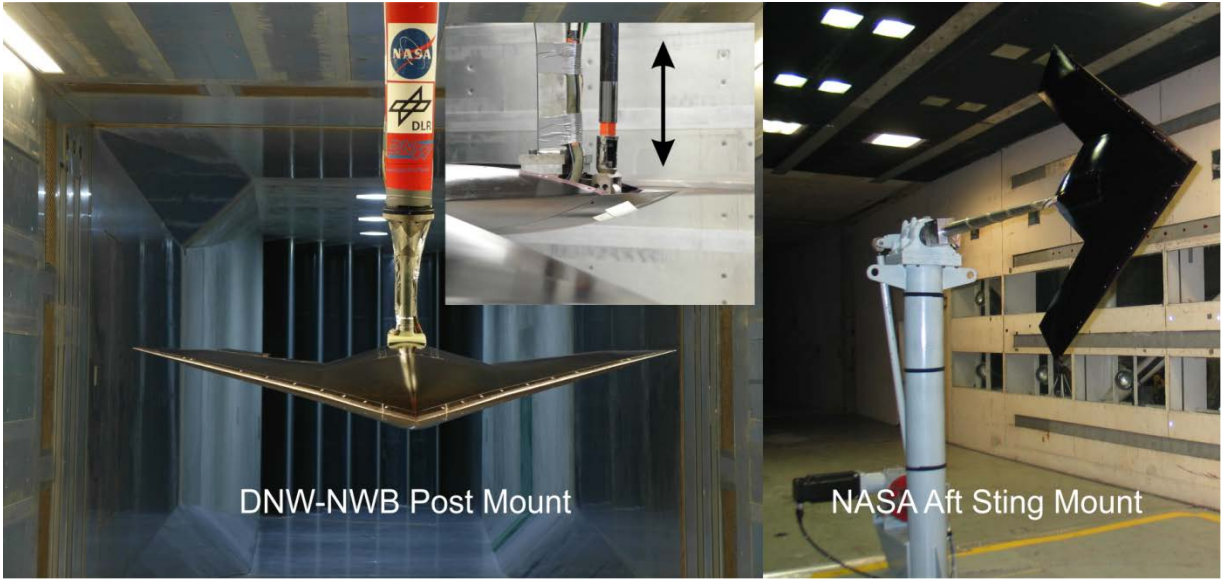
Figure 17.   Roll-oscillation mounting arrangements in the DNW-NWB and NASA Tunnels.
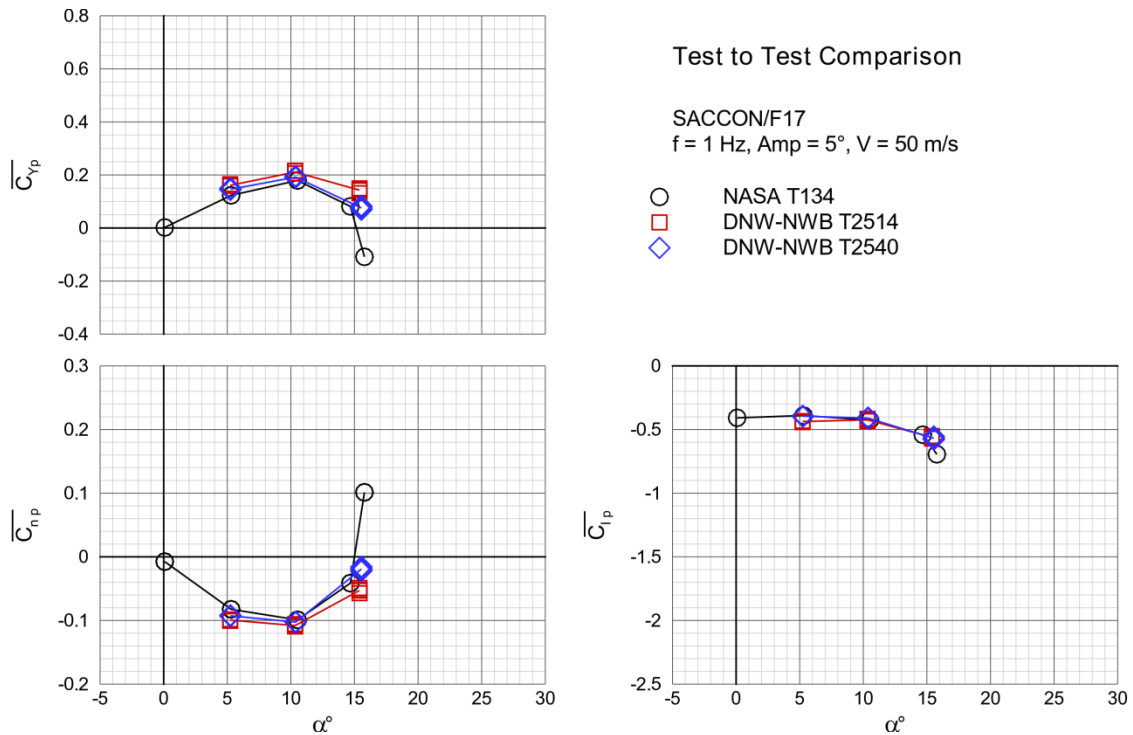

Figure 18.   Comparison of roll axis dynamic derivatives for 1 Hz oscillation frequency.

G. Effect of rotation origin

The aft location of the belly-sting mount was intentionally selected to minimize the influence of the sting on the overall flow topology and reduce the pitching moment load imposed on the balance. This aft mounting arrangement however resulted in the default rotation axis of the forced oscillation being well aft of the likely center of rotation of the vehicle. The sensitivity of the dynamic derivatives to the center or rotation location is a question that often arises in forced oscillation testing. Often the limitations of the test rig facilitates only testing about at fixed rotation point, whereas the center of rotation of the vehicle can vary with changes in the center of gravity. The MPM system provides the capability to change the center of rotation and provide some insight into this question. A series of pitch

American Institute of Aeronautics and Astronautics

and yaw oscillations were conducted with the center of rotation at two different origins. One was about the aft mounting location and the other was about the moment reference center, as shown in figure 2.

The effect of the rotation origin on the pitch and yaw dynamic derivatives are shown in figures 19 and 20, respectively. The pitch axis offset shows a shift in the normal $(\overline{C_{N_q}})$ and axial $(\overline{C_{A_q}})$ derivatives but surprisingly little if any change in the pitch damping derivative $(\overline{C_{m_q}})$. The yaw axis offset showed only a slight increase in the roll derivative $(\overline{C_{l_r}})$. The insensitivity in the yaw axis is not surprising since this is a tailless configuration without any vertical surfaces. One would expect the rotation axis location to have a more pronounced effect on configurations with tails and vertical surfaces. The ability of the MPM to explore this effect will perhaps provide greater insight into its sensitivity for various configurations.

H. Effect of control surface chord length

One of the primary differences between F17/SACCON and the F19 models was the chord length of the control surfaces. The F17/SACCON had control surfaces that were 20% of the wing chord whereas the F19 had two sets of controls surfaces that were 20% or 25% of the wing chord. An investigation of the effect of the control surface chord length on the dynamic derivatives was conducted with the F19 model. A series of pitch and yaw oscillation runs with the left outboard control surface split-deflected ±20° were conducted with 20% and 25% chord control surfaces. The results are presented in figures 21 and 22 for the pitch and yaw oscillations at frequencies of 1 and 2 Hz. The figures show that for this control surface deflection the frequency had a much larger effect on the dynamic derivatives than the chord wise length of the control. Only the pitch damping $(\overline{C_{m_q}})$ and yaw damping $(\overline{C_{n_r}})$ terms at 20° angle of attack showed any appreciable variation with chord length.
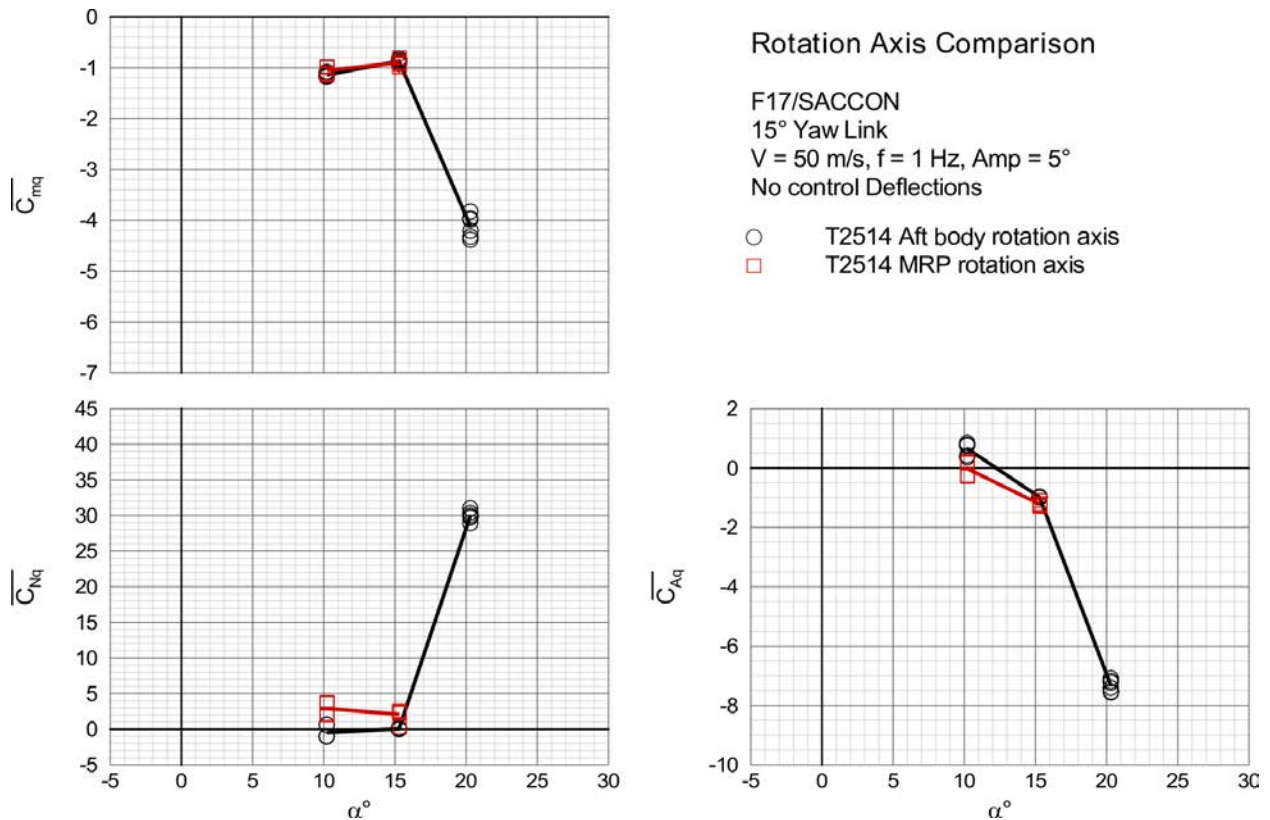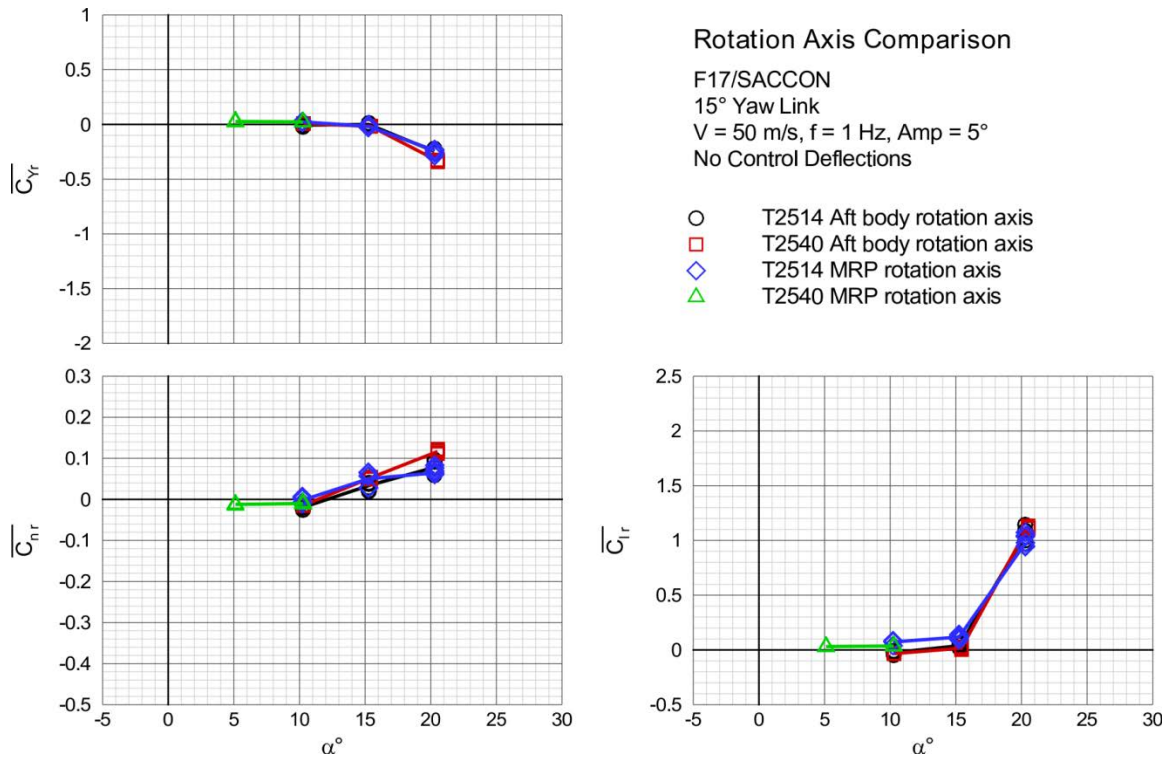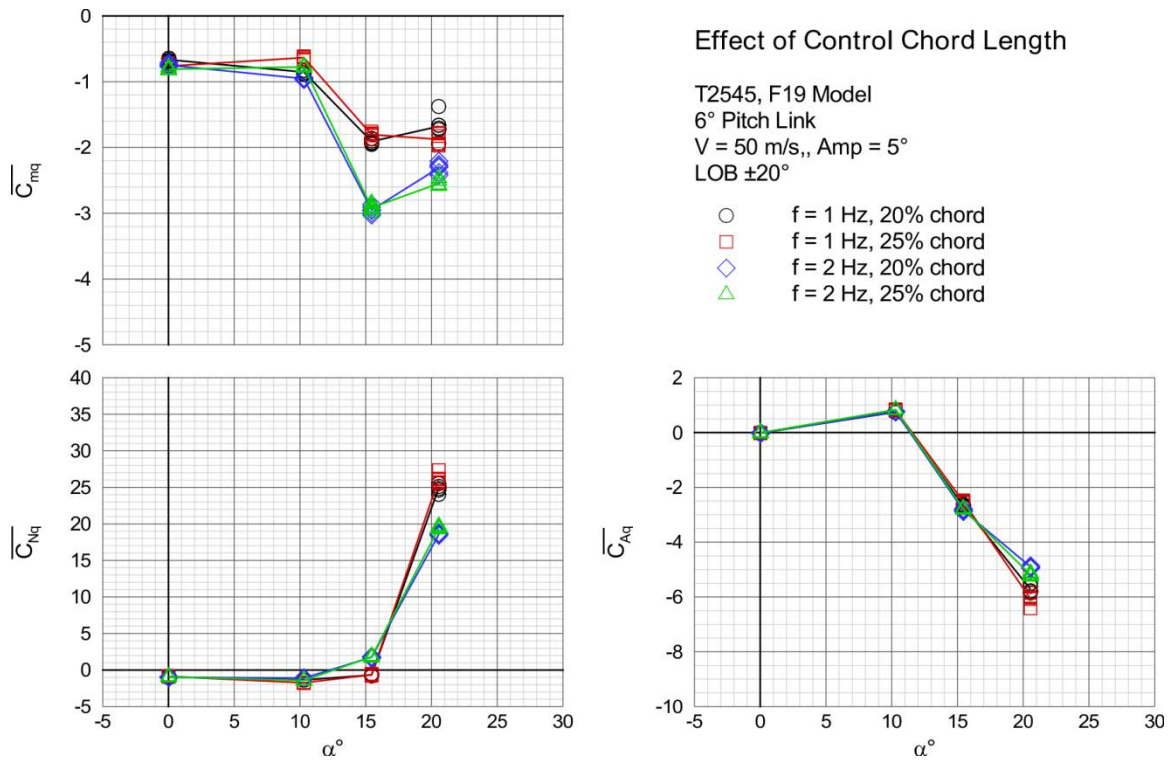

Figure 19. **Effect of rotation axis location on pitch axis dynamic derivatives**
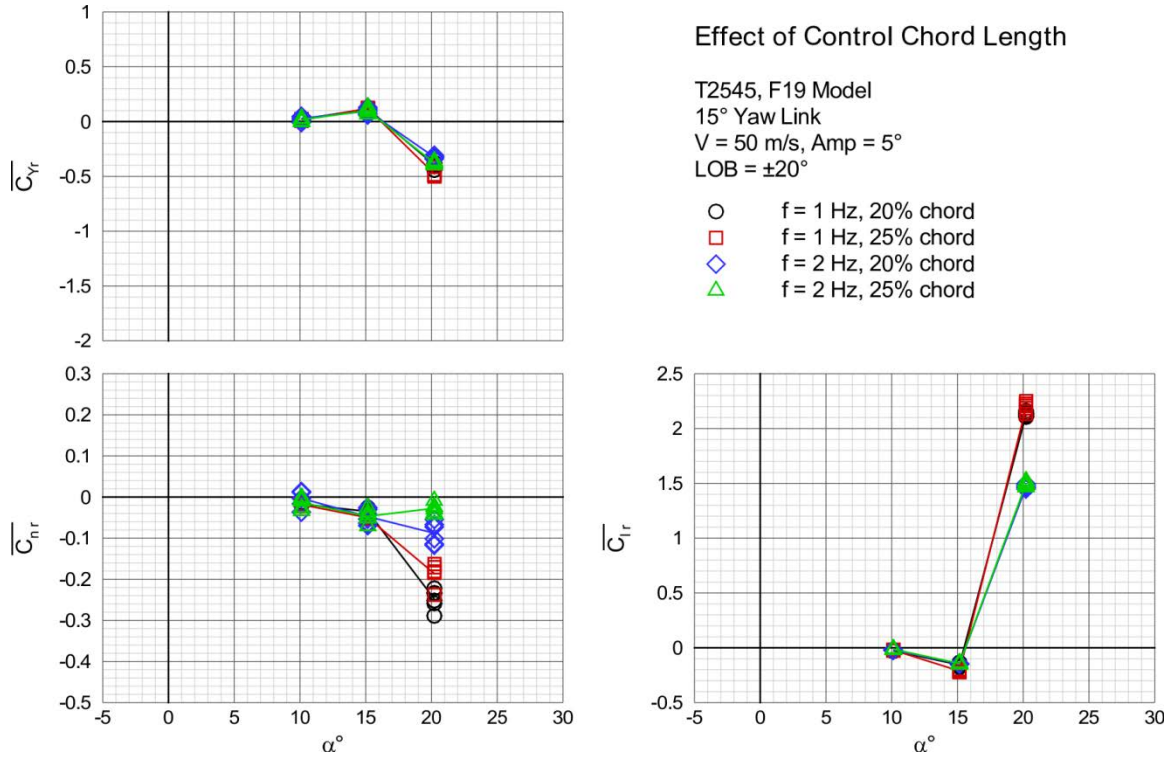
Figure 20.   Effect of rotation axis location on yaw axis dynamic derivatives.

Figure 21.   Effect of control chord length on pitch axis dynamic derivatives.

American Institute of Aeronautics and Astronautics

Figure 22.   Effect of control chord length on yaw axis dynamic derivatives.

I. Common Test Cases

A limited set of the DLR-F19 static and dynamic experimental data were selected by the AVT-201 group as the focus of their CFD analysis and comparisons. The matrix of these selected dynamic pitch and yaw common test cases is presented in Tables 2 and 3, respectively. All of the common test case runs were with the 25% chord controls surfaces. The results are presented here for reference in AVT-201 CFD analysis papers.

The common test case pitch and yaw dynamic derivatives are presented in figures 23 and 24, respectively. The figures show that the large roll control deflection has a negligible effect on the dynamic derivatives below 15° angle of attack. The effect of the control deflections at the higher angles of attack are most readily apparent in the pitch-damping derivative ($\overline{C_{m_q}}$) but are of similar magnitude as the frequency effect.

Table 2. DLR-F19 dynamic pitch common test case matrix.

Runs	Control Deflection, deg					V,	θ_0,	Amp,	f,
		LOB	LIB	RIB	ROB	m/s	deg	deg	Hz
2345-50		0	0	0	0	50	10	4.7	1.00
2354-59		0	0	0	0	50	10	4.7	2.00
2669-74		-20	-20	+20	+20	47	10	4.7	0.94
2678-83		-20	-20	+20	+20	47	10	4.7	1.88
2363-68		0	0	0	0	50	15	4.7	1.00
2372-77		0	0	0	0	50	15	4.7	2.00
2651-56		-20	-20	+20	+20	47	15	4.7	0.94
2660-65		-20	-20	+20	+20	47	15	4.7	1.88

Table 3. DLR-F19 dynamic yaw common test case matrix.

Runs	Control Deflection, deg					V, m/s	θ_0, deg	Amp, deg	f, Hz
		LOB	LIB	RIB	ROB				
2273-78		0	0	0	0	50	10	5	1.00
2282-87		0	0	0	0	50	10	5	2.00
2165-70		-20	-20	+20	+20	47	10	5	0.94
2174-79		-20	-20	+20	+20	47	10	5	1.88
2291-96		0	0	0	0	50	15	5	1.00
2300-05		0	0	0	0	50	15	5	2.00
2183-88		-20	-20	+20	+20	47	15	5	0.94
2192-97		-20	-20	+20	+20	47	15	5	1.88

Figures 25-32 show the 1-cycle average hysteresis loops with the standard deviation bars for all of the common test case runs. Six runs were conducted for each common test case condition. The 1-cycle average hysteresis loops show very good repeatability between runs. The effect of the control deflections is clearly seen in the lateral/directional coefficient hysteresis loop offsets. The complex flow characteristics at 15° angle of attack are also evident in the pitch hysteresis loops shown in figures 27 and 28. Replicating these complex hysteresis loops and the associated relevant flow physics through CFD methods is one of the challenges facing the AVT-201 group.
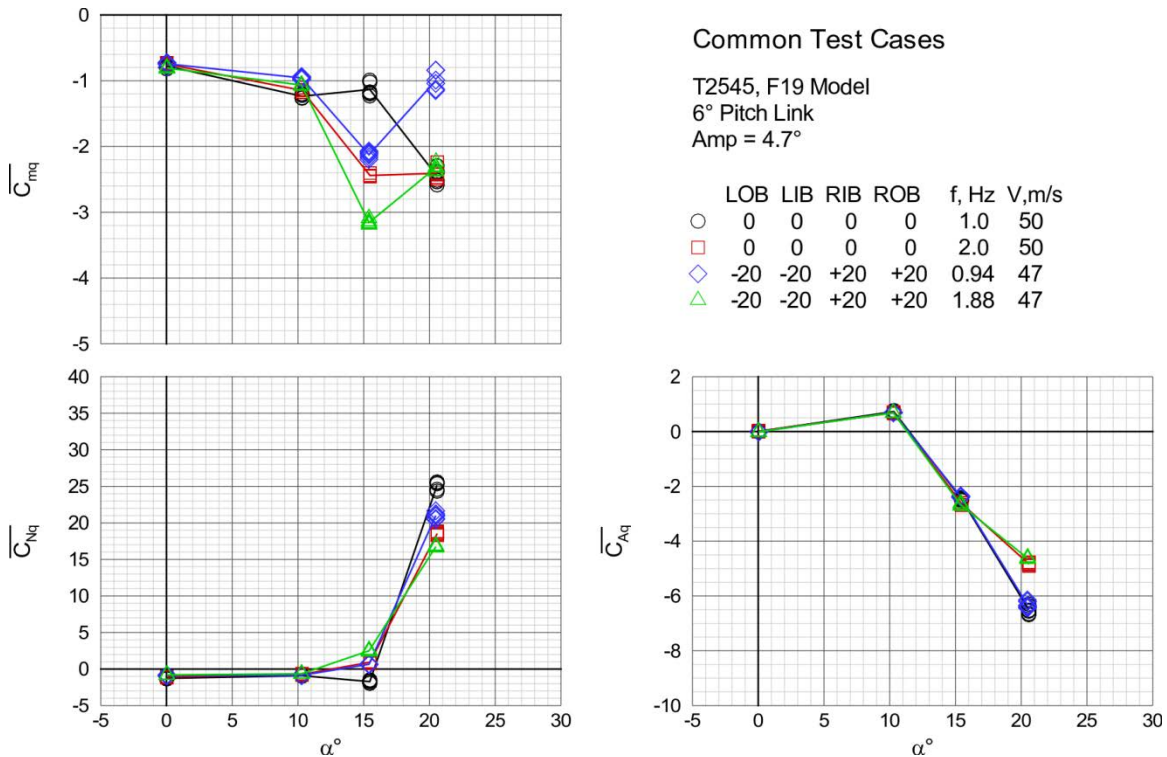

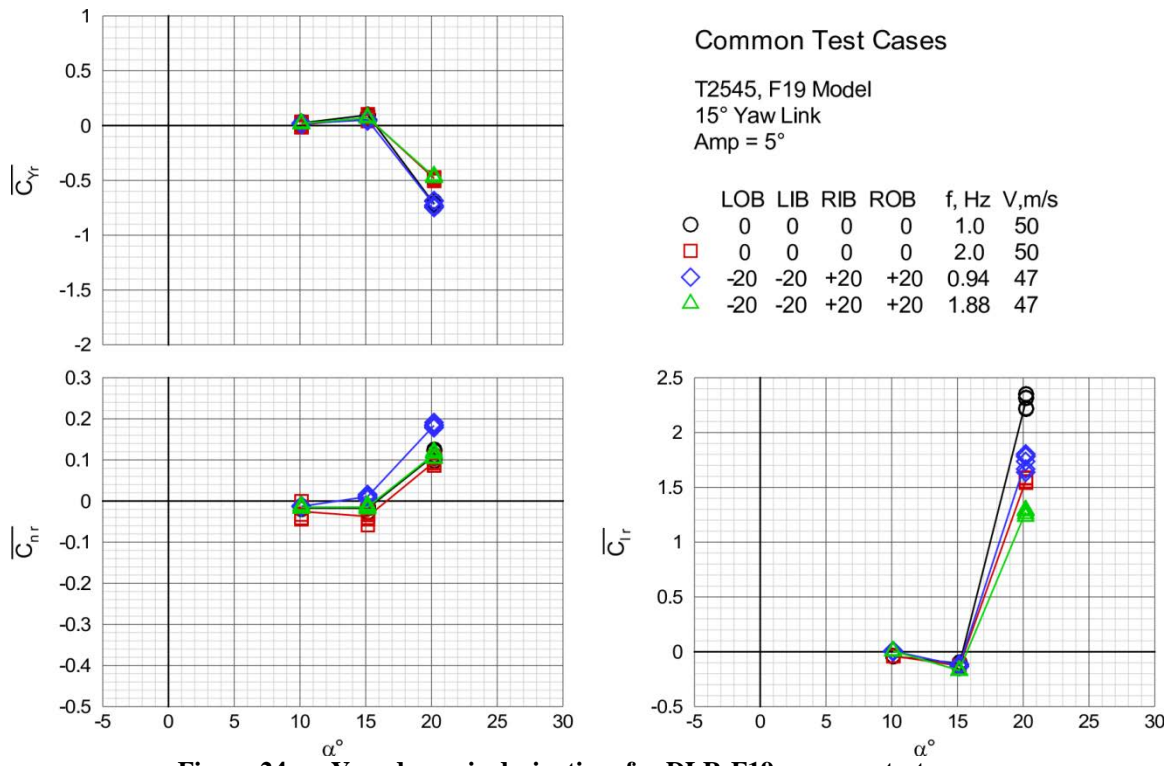**Figure 23.   Pitch dynamic derivatives for DLR-F19 common test cases.**

Figure 24.   Yaw dynamic derivatives for DLR-F19 common test cases.
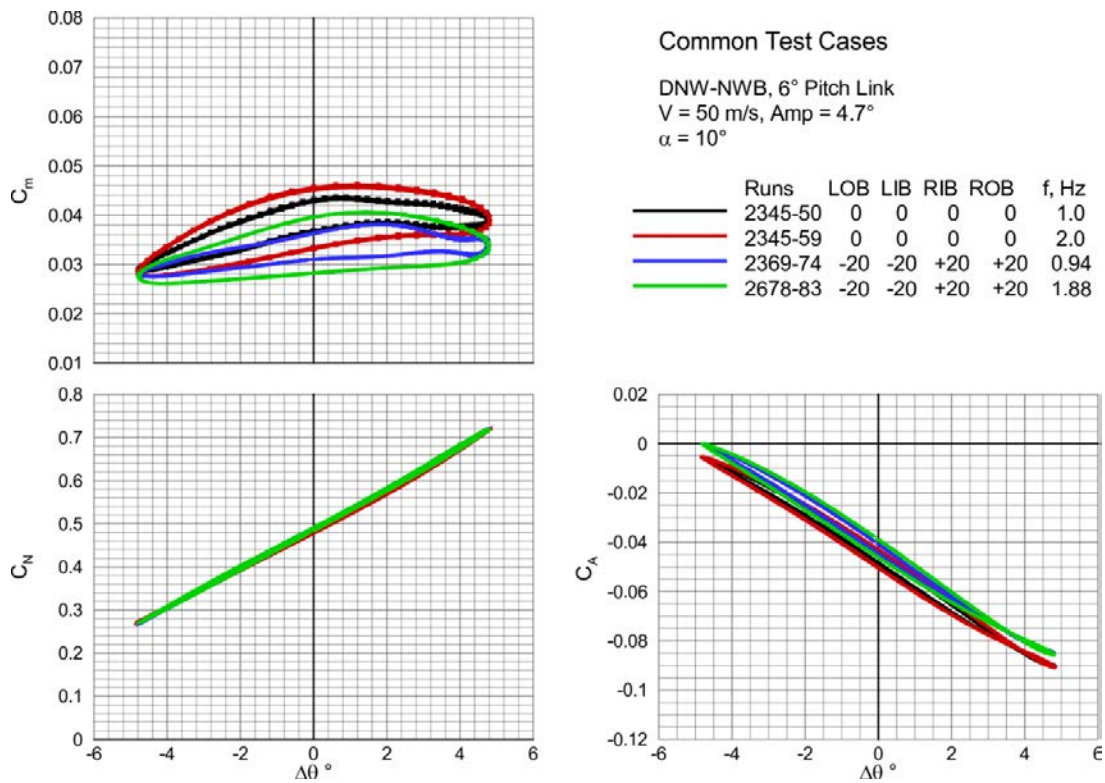

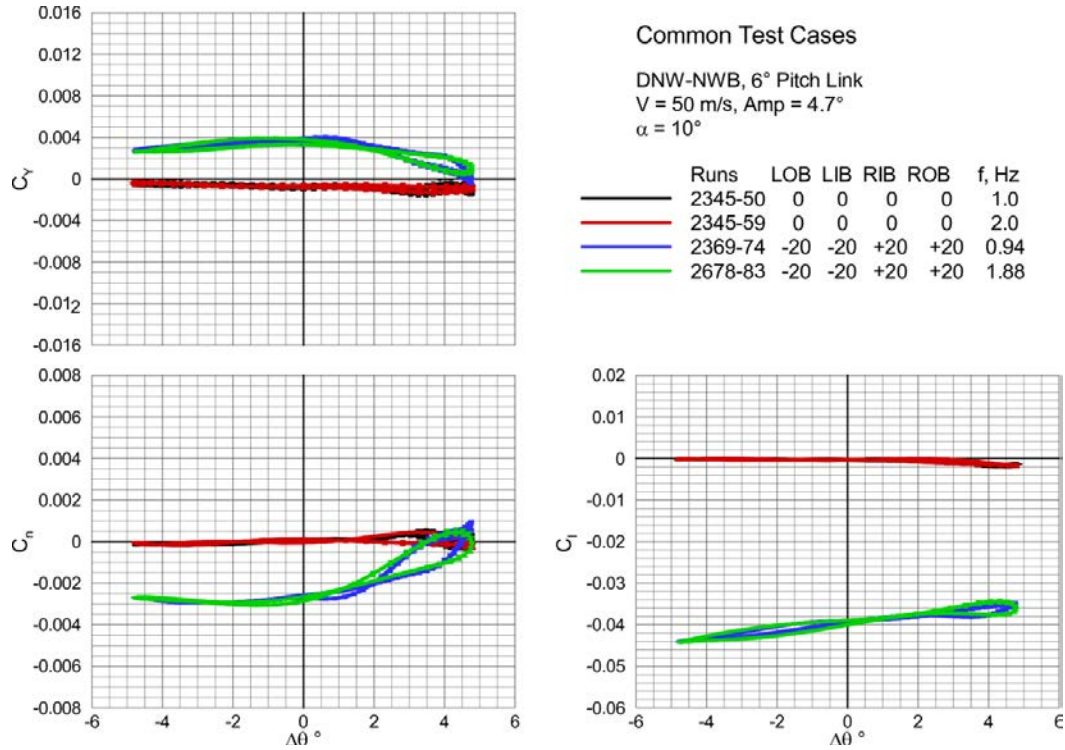**Figure 25.   Common test cases longitudinal coefficient 1-cycle average pitch hysteresis loops for 10° angle of attack.**

Figure 26. Common test cases lateral/directional coefficient 1-cycle average pitch hysteresis loop for 10° angle of attack.
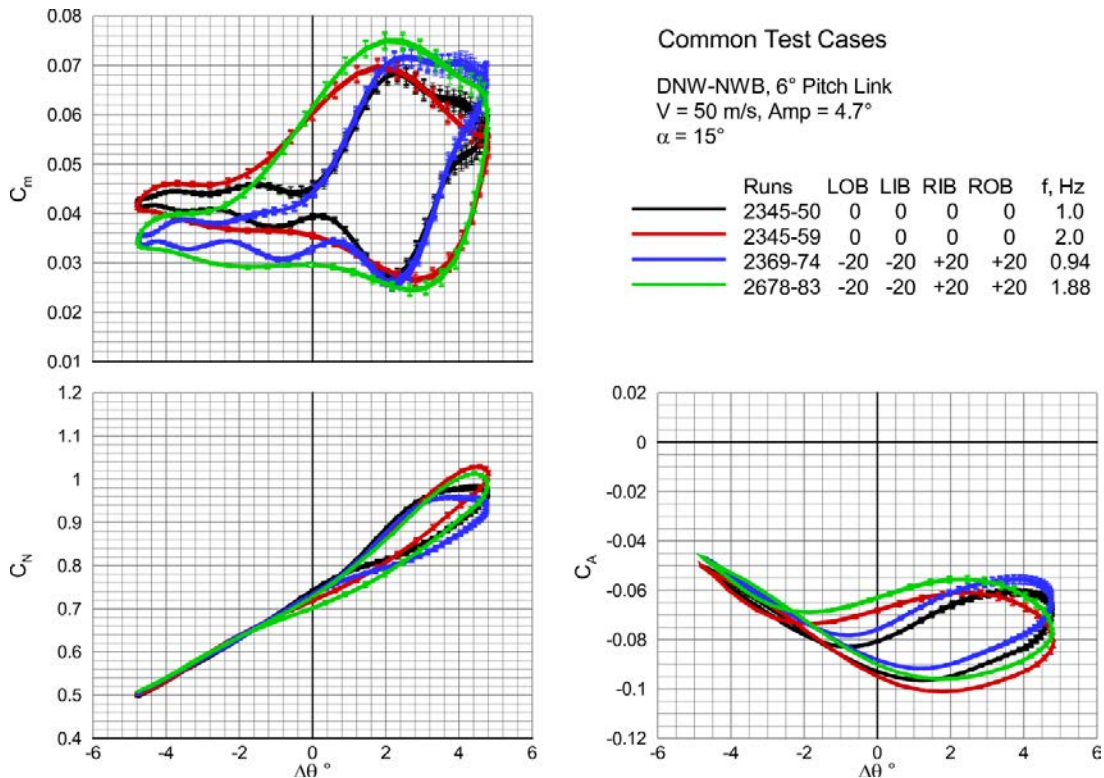

Figure 27. Common test cases longitudinal coefficient 1-cycle average pitch hysteresis loops for 15° angle of attack.

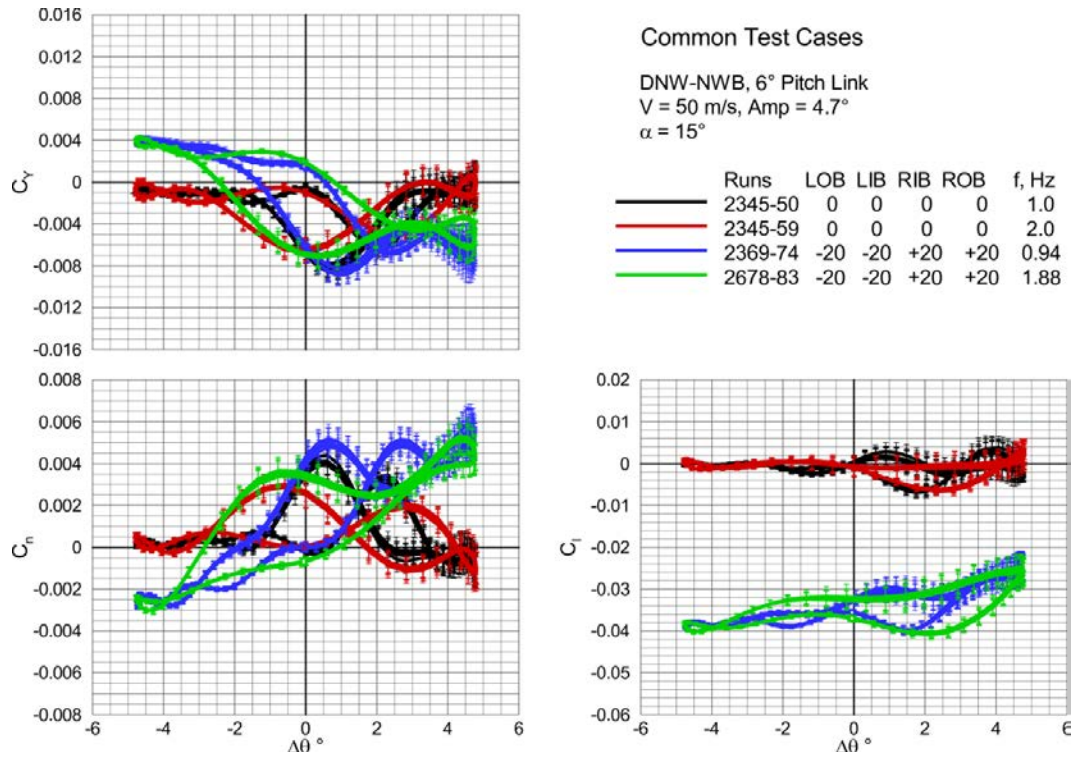American Institute of Aeronautics and Astronautics

Figure 28. Common test cases lateral/directional coefficient 1-cycle average pitch hysteresis loop for 15° angle of attack.

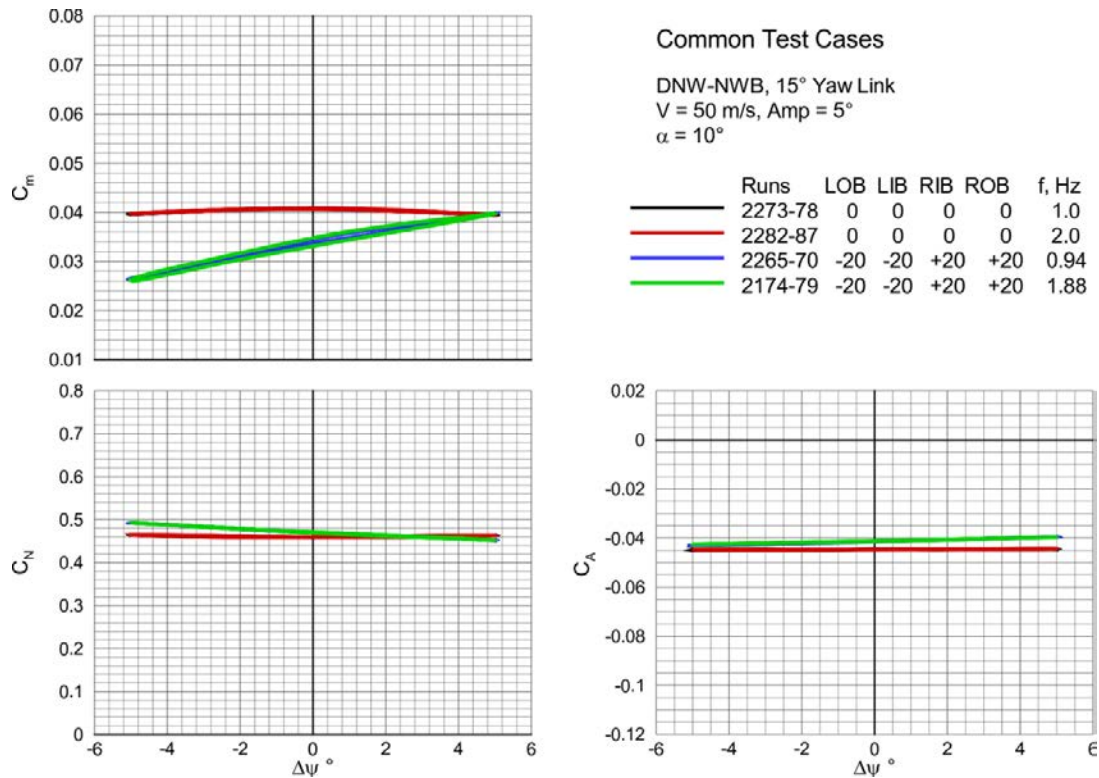

Figure 29. Common test cases longitudinal coefficient 1-cycle average yaw hysteresis loops for 10° angle of attack.

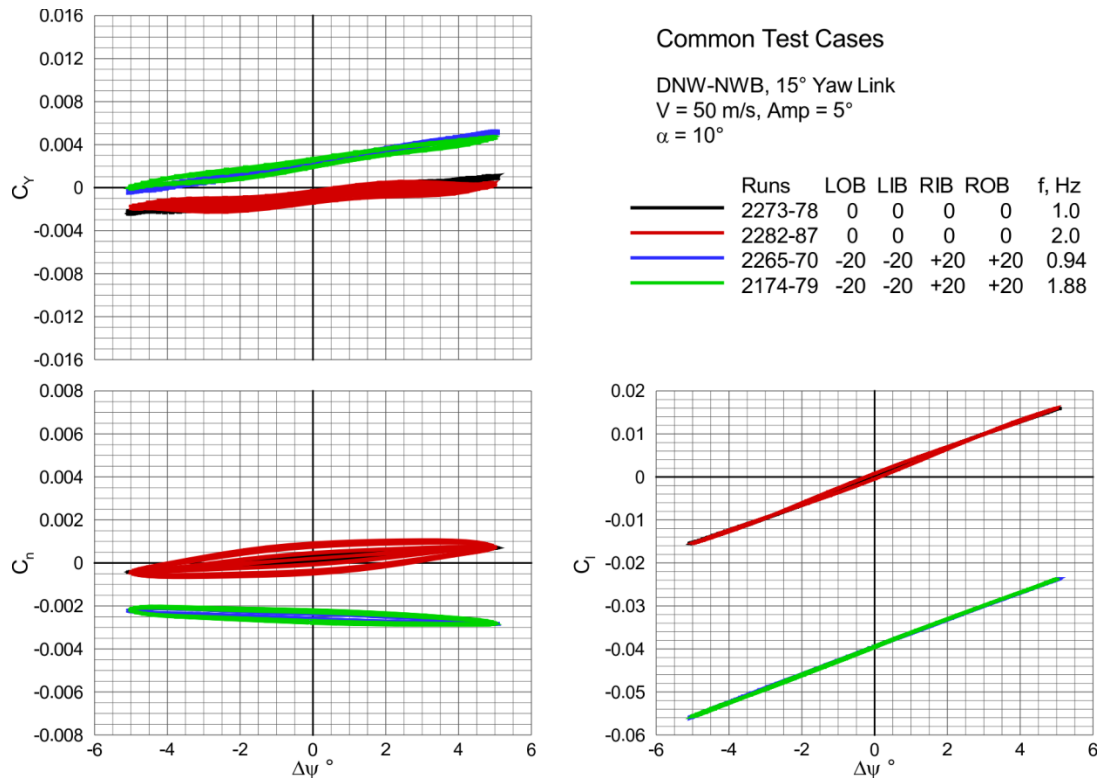American Institute of Aeronautics and Astronautics

**Figure 30.   Common test cases lateral/directional coefficient 1-cycle average yaw hysteresis loops for 10°
angle of attack.**

**Figure 31.   Common test cases longitudinal coefficient 1-cycle average yaw hysteresis loops for 15° angle of
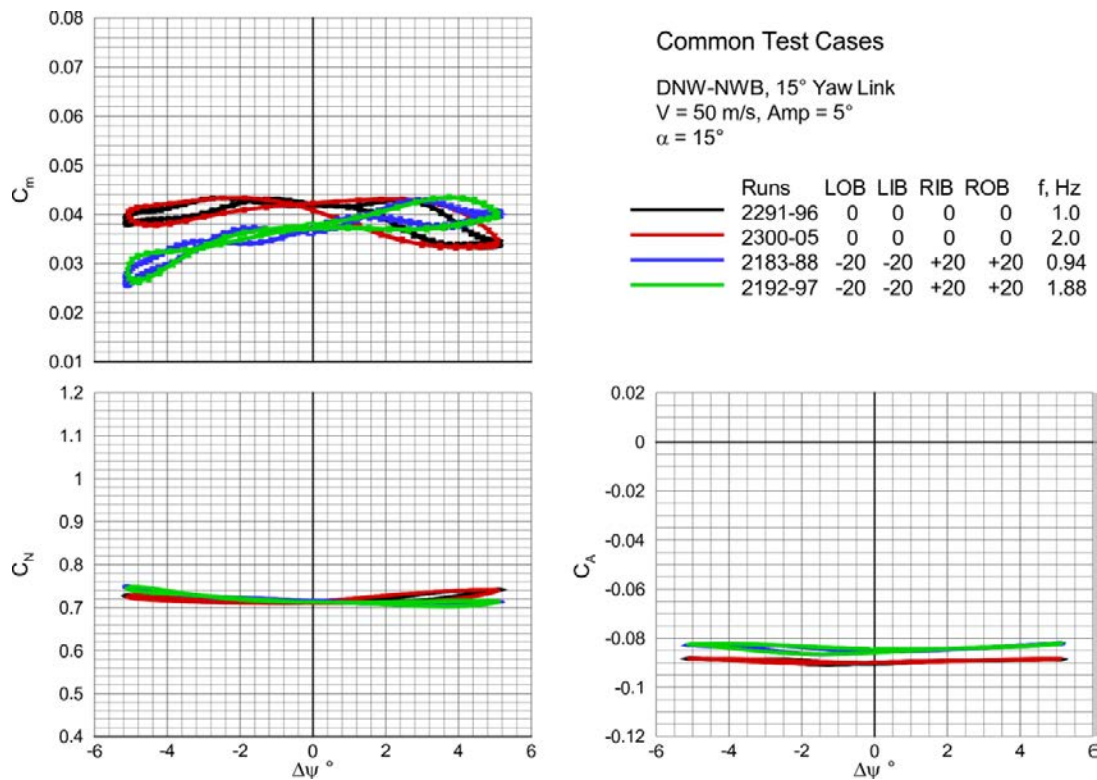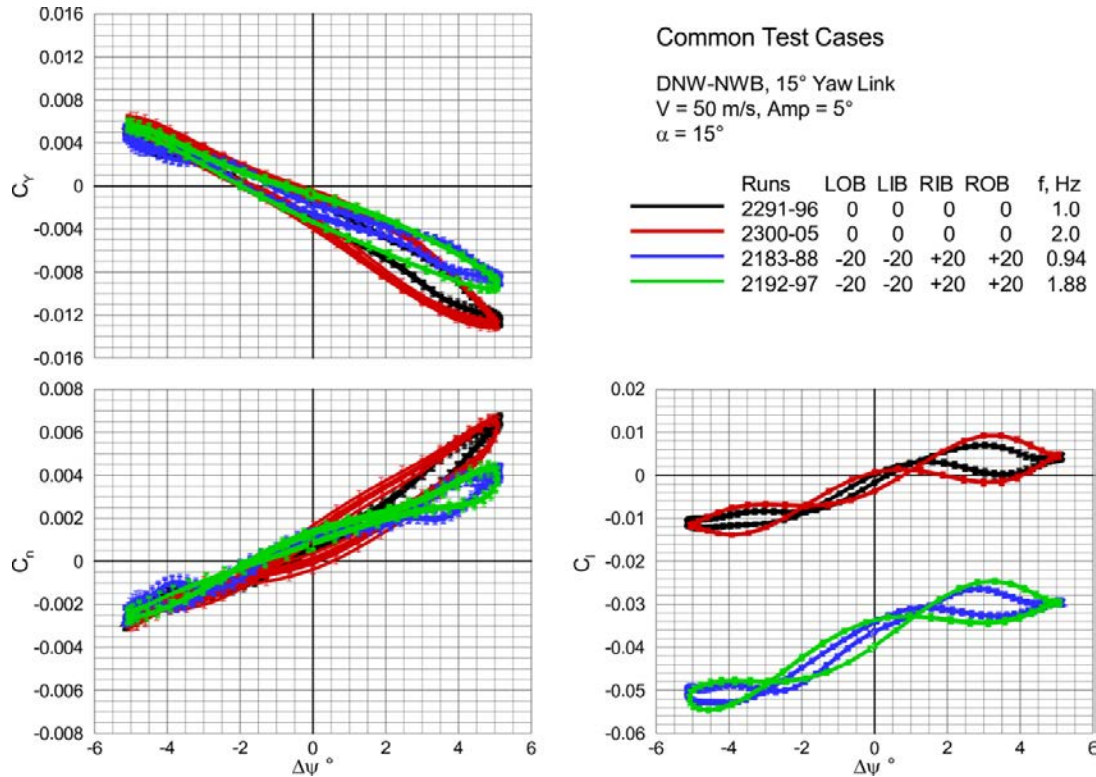attack.**

American Institute of Aeronautics and Astronautics

Figure 32. **Common test cases lateral/directional coefficient 1-cycle average yaw hysteresis loops for 15°**
angle of attack.

J. Dynamic Maneuver Cases

As previously noted the dynamic pitch maneuver data was collected for a DLR research project in advanced dynamic modeling and parameter identification and was not originally intended for inclusion in this paper. However, a simple linear dynamics model was fit to these maneuver datasets and yielded useful results for this AVT-201 research. The more advanced system identification research for which this data was collected will be reported in future DLR publications.

The results of the simple model fit to the appended maneuver time history files are presented in figure 33. The model fit comparison to both the static and dynamic longitudinal coefficient data show very good agreement below 15° angle of attack. This was also previously shown in the fit residuals plot in figure 10. At the higher angles of attack where the flow is separated the simple linear model (eq. 5) is not sufficient to model the flow characteristics. In this region more complex non-linear modeling methods are required.

One of the advantages of this dynamic maneuver experimental technique is illustrated in the dynamic derivative values shown in the right column of figure 33. The classic sinusoidal forced oscillation method provides a derivative value at a fixed angle-of-attack. To generate values over an angle of attack range requires many runs. With a dynamic maneuver run you can collect both the static and dynamic longitudinal data that would traditionally take many data runs. In this particular case the appended dynamic maneuver run was 70 seconds. To collect the same data from a static angle of attack sweep (30 points at 2sec/point) and sinusoidal oscillations at each angle of attack and two frequencies (60 points at 30sec/point) is 1860 seconds without including transition times between points. That is a 96% improvement test time efficiency. Developing the dynamic maneuvers and analysis to optimize the system identification process is an area of ongoing research.
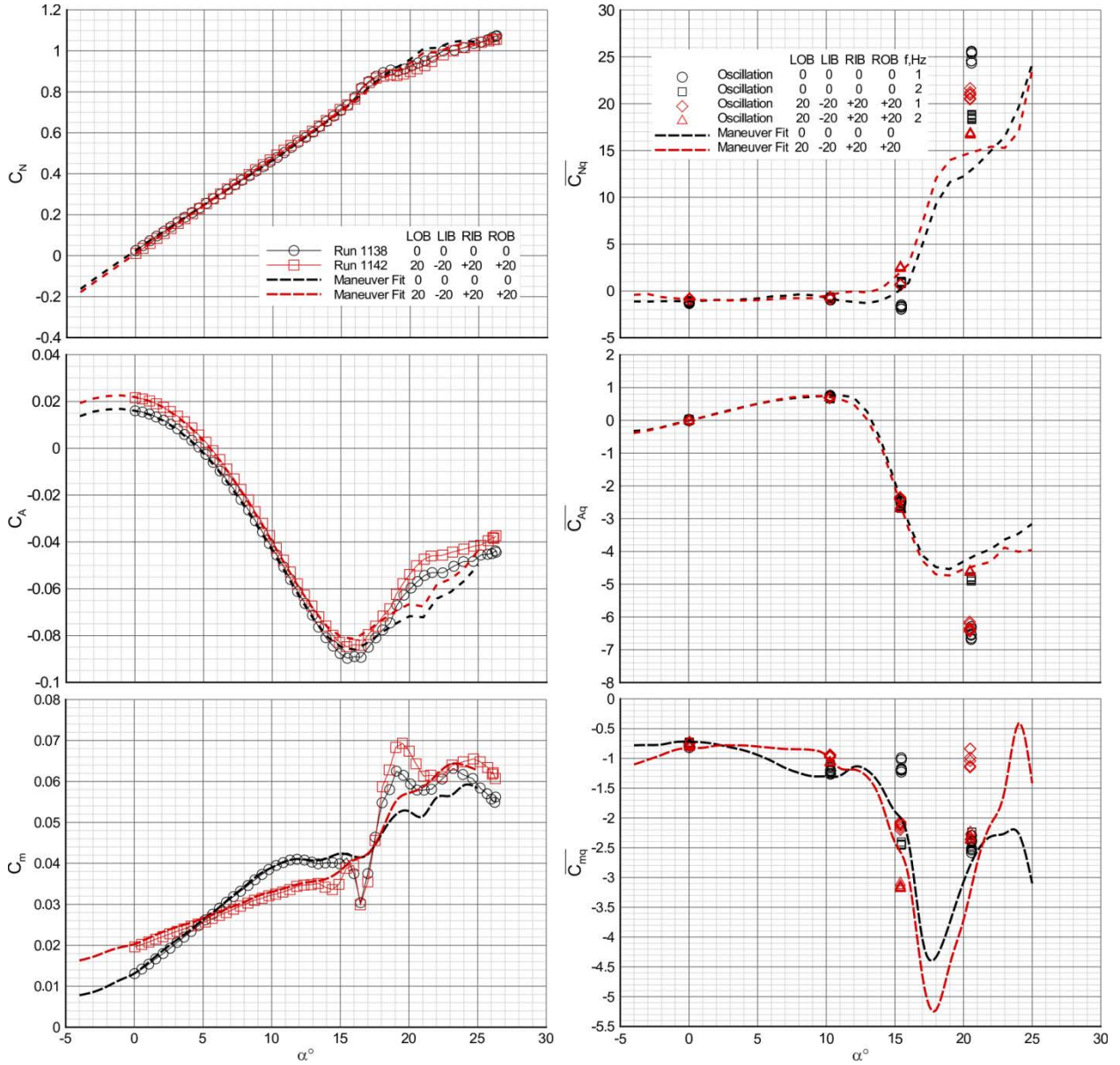
American Institute of Aeronautics and Astronautics

Figure 33. Dynamic pitch maneuver model fit results.

IV.

V. Concluding Remarks

Significant low-speed dynamic datasets of the F17/SACCON and F19 models have been collected for the purpose of CFD validation. Test-to-test, tunnel-to-tunnel and model-to-model comparisons showed only slight differences in the dynamic derivatives with the largest variations occurring in the separated flow region of 15° angle of attack and above. A subset of F19 common test cases were selected for focused CFD analysis and comparisons. The dynamic derivatives and 1-cycle averaged hysteresis loops for those common test cases are presented here for reference.

Investigations into the effect of the pitch and yaw rotation axes on the dynamic derivatives showed an effect on the normal and axial pitch derivatives but surprisingly little if any change in the pitch damping derivative. The yaw axis offset showed only a slight increase in the roll derivative. The insensitivity in the yaw axis is likely due to this being a tailless configuration without any vertical surfaces.

The investigation into the effect of the chord wise length of the control surface on the dynamic derivatives showed that the frequency variation had a much larger effect on the dynamic derivatives than the chord wise length of the control.

The analysis of the simple model fit to the dynamic pitch maneuver showed that fit provided very good agreement to both the static and dynamic longitudinal coefficient data below 15° angle of attack. At the higher angles of attack where the flow is separated the simple linear model was not sufficient to model the flow characteristics. The dynamic maneuver analysis also highlighted the potential test efficiency improvement provided through this test technique.

References

[1]Schütte, A.; Cummings, R.; Loeser, T.; and Vicroy, D.: "Integrated Computational/Experimental Approach to UCAV and Delta-Canard Configurations Regarding Stability & Control," *4th Symposium on Integrating CFD and Experiments in Aerodynamics*, Von Karman Institute, Rhode-Saint-Genèse, Belgium, September 14-16, 2009.

[2]Cummings, R.; and Schütte, A.: "Computational/Experimental Approach to UCAV Stability & Control Estimation: Overview of NATO RTO AVT-161," AIAA 2010 4392, *28th AIAA Applied Aerodynamics Conference*, Chicago, IL, June 28 – July 1, 2010.

[3]Loeser, T.; Vicroy, D.; and Schütte, A.: "SACCON Static Wind Tunnel Tests at DNW-NWB and 14'x22' NASA LaRC," AIAA 2010 4393, *28th AIAA Applied Aerodynamics Conference*, Chicago, IL, June 28 – July 1, 2010.

[4]Vicroy, D.; Loeser, T.; and Schütte, A.: "SACCON Forced Oscillation Tests at DNW-NWB and NASA Langley 14x22-foot Tunnel," AIAA 2010 4394, *28th AIAA Applied Aerodynamics Conference*, Chicago, IL, June 28 – July 1, 2010.

[5]Gilliot, A.: "Static and Dynamic SACCON PIV Tests – Part I: Forward Flow Field," AIAA 2010 4395, *28th AIAA Applied Aerodynamics Conference*, Chicago, IL, June 28 – July 1, 2010.

[6]Konrath, R.; Roosenboom, E.; Schröder, A.; Pallek, D.; and Otter, D.: "Static and Dynamic SACCON PIV Tests – Part II: Aft Flow Field," AIAA 2010 4396, *28th AIAA Applied Aerodynamics Conference*, Chicago, IL, June 28 – July 1, 2010.

[7]Schütte, A; Hummel, D.; and Hitzel, S., "Numerical and Experimental Analyses of the Vortical Flow Around the SACCON Configuration," AIAA 2010 4690, *28th AIAA Applied Aerodynamics Conference*, Chicago, IL, June 28 – July 1, 2010.

[8]Cummings, R. M.; Schütte, A.; et al.: Summary Report of the NATO RTO/AVT-161 Task Group on "Assessment of Stability and Control Prediction Methods for NATO Air and Sea Vehicles", RTO-TR-AVT-161 AC/323(AVT-161)TP/440, September 2012.

[9]Rohlf, Detlef; Schmidt, Stefan and Irving, Jonathan: "Stability and Control Analysis for an Unmanned Aircraft Configuration Using System-Identification Techniques," *Journal of Aircraft*, Vol. 49, No. 6, 2012, pp 1597-1609, doi: 10.2514/1.C031392.

[10]Huber, K. C.; Vicroy, D. D.; Schütte, A.; and Huegner, A.: "UCAV model design and static experimental investigations to estimate control device effectiveness and S&C capabilities", *32nd AIAA Applied Aerodynamics Conference*, Atlanta, GA, June 16–20, 2014 (submitted for publication).

[11]Kausche, G. et al., "The Low-Speed Wind Tunnel at DFVLR in Brunswick (Status 1988)", DFVLR-Mitt. 88-25 (1988)

[12]Bergmann, A.: "The Model Positioning Mechanism of DNW-NWB Based on a New Parellel Kinematic," Open Technology Forum, Aerospace Testing Expo, Hamburg, Germany, April 2005.

[13]Bergmann, A.; Huebner, A.; and Loeser, T.: "Experimental and numerical research on the aerodynamics of unsteady moving aircraft," *Progress in Aerospace Sciences*, vol. 44, issue 2, February, 2008, pp. 121-137.

[14]Brandon, J. M.; Foster, J. V.: "Recent Dynamic Measurements and Considerations for Aerodynamic Modeling of Fighter Airplane Configurations," AIAA 98-4447, August 10-12, 1998.

[15]Brandon, J. M.; Foster, J. V.; Gato, W.; and Wilborn, J. E.: "Comparison of Rolling Moment Characteristics During Roll Oscillations for a Low and a High Aspect Ratio Configuration," AIAA 2004-5273, *AIAA Atmospheric Flight Mechanics Conference and Exhibit*, Providence, RI, August 16-19, 2004.